



3D velocity and anisotropy of the southeastern Tibetan plateau extracted by joint inversion of wave gradiometry, ambient noise, and receiver function

Feihuang Cao ^{a,b}, Chuntao Liang ^{a,b,*}, Yihai Yang ^c, Lu Zhou ^{a,b}, Zhiqiang Liu ^{a,b}, Zhen Liu ^{a,b}

^a Key Laboratory of Earth Exploration and Information Techniques of the China Ministry of Education, Chengdu, China

^b State Key Laboratory for Oil and Gas Reservoir Geology and Exploitation, Chengdu University of Technology, Chengdu, China

^c Shaanxi Earthquake Agency, Xi'an, Shanxi, China

ARTICLE INFO

Keywords:

Wave Gradiometry
Joint Inversion
Anisotropy
Tibetan Plateau
Geodynamics

ABSTRACT

With the deformation pattern of the southeastern Tibetan Plateau remaining controversial, its anisotropic structure and the three-dimensional (3D) velocity model are powerful tools for understanding this issue. The surface wave dispersion curve (DC) and receiver function (RF) are sensitive to absolute velocity and elasticity contrasts, respectively. In this work, we propose a new method for the joint inversion of 3D shear velocity (V_s) and anisotropy using the datasets of RFs and DCs, which are obtained by combining the wave gradiometry method and ambient noise tomography. Because DCs and RFs are divided into back-azimuth bins, and both datasets in each bin are jointly inverted to obtain velocity in the corresponding direction, the method is called the azimuth-dependent joint inversion method. By applying this new method to the Temporary West Sichuan Array, we obtained a high-resolution 3D V_s model and anisotropic structure of the southeastern Tibetan Plateau. In our model, the vertically consistent fast propagation direction in the Songpan-Ganzi block (SGB) and the north Chuandian block (NCDB) suggest that the deformation in this region is largely coupled vertically. Our model provides anisotropic evidence of the Yangtze crystalline basement extending to the SGB. The low-velocity zone (LVZ) was much thicker and more prominent in the NCDB than in the SGD. Anisotropy in the middle lower crust of the NCDB does not show any sign of an LVZ flowing from the SGB or the Qiangtang block to the NCDB. These observations are contrary to those of the crust flow model, suggesting that the LVZ was generated locally. The mushroom-shaped high-velocity structure beneath the southern Chuandian block and boundary fault zone may be a relic of the Emeishan paleo-mantle plume.

1. Introduction

The Tibetan Plateau, located in western China, is known as the roof of the world owing to its high altitude. The Indian–Eurasian collision created magnificent natural landscapes along with life-threatening earthquakes when the Indian plate moved northward and collided with the Eurasian plate in the Eocene, resulting in the closure of the new Tethys Ocean (Molnar and Tapponnier, 1975; Rowley, 1996). Under the subduction of the Indian Plate and the blocking of the Tarim Basin and the Alxa Block, the Tibetan Plateau has been squeezing, shortening, and moving northeastward (Yin and Harrison, 2000; Tapponnier et al., 2001; Gan et al., 2007; Zhao et al., 2015). Owing to the blocking of the Sichuan Basin and Ordos Block, the material is diverted to the northeast and southeast (Gan et al., 2007; Xu et al., 2003; Zhang et al., 2013) and is blocked again by the Emeishan large igneous province (ELIP) (Ni

et al., 1989; Li et al., 2008; Li et al., 2020; Zhang et al., 2020; Liang et al., 2020; Liu et al., 2021a, 2021b). The southeastern Tibetan Plateau (Fig. 1), one of the areas with the strongest tectonic movements in China, is a key area for studying the deformation mechanism of the Tibetan Plateau. Influenced by the far-field effect of the India–Eurasia collision and the subduction of the Burmese microplate, strong seismic activity, complex fault systems (Zhang, 2008; Xu et al., 2003), craggy mountains, and deep valleys appear in this region (Tapponnier and Molnar, 1977; Searle et al., 1987; Xu et al., 2003; Li et al., 2014a, 2014b). However, the deformation pattern of the Tibetan plateau is still debated, with two main models being used to explain the plateau uplift: (1) the pure shearing model—plateau uplift is dominated by the pure-shear shortening and thickening of the crust or whole lithosphere (Tapponnier and Molnar, 1977; Tapponnier et al., 1982; Yin, 2010; Robert et al., 2010), in this case, the eastern Tibetan upper crust is thrust

* Corresponding author at: Key Laboratory of Earth Exploration and Information Techniques of the China Ministry of Education, Chengdu, China.
E-mail address: liangct@cdut.edu.cn (C. Liang).

over the Sichuan basin; and (2) the mid-lower crust flow model—the vertical expansion in the viscous mid-lower crust is the main reason of plateau uplift (Clark et al., 2004; Klemperer, 2006; Bai et al., 2010; Yin, 2010). In addition, Gan et al. (2007) suggest that the pure-shear shortening and thickening plays a greater role in the early period of the Indian-Eurasian collision, because the crust might not have been thickened enough to develop the crustal channel flow; in the later stage, the crustal viscous flow dominates crustal deformation.

The seismic velocity model and anisotropic structure can provide valuable information on present and past tectonic evolution. The surface wave dispersion curve (DC) and receiver function (RF) are typically used to invert the shear wave velocity (V_s) and anisotropy. In recent decades, many surface-wave data processing techniques have been proposed. For example, the two station method (Campillo and Paul, 2003) uses the travel time between two stations to estimate seismic velocity — the

resolution is dependent on the density of raypath, and the two stations need to be aligned along the raypath i.e., more earthquakes are needed to improve the coverage of raypath; the two plane wave method (Forsyth et al., 1998; Yang and Forsyth, 2006) can solve the phase velocity and azimuthal variation of earthquakes; eikonal tomography (Lin et al., 2009) computes the phase velocity by solving the travel time of dense array; Helmholtz tomography (Lin and Ritzwoller, 2011) is similar to eikonal tomography, but an amplitude correction for reducing the effect of back scattering is taken into account; and wave gradiometry method (WGM) links the seismic wave gradient to the phase velocity, azimuth, geometrical spreading, and the radiation pattern (Langston, 2007c; Liang and Langston, 2009a). The Rayleigh wave obtained from cross-correlating ambient noise is more robust at periods shorter than 30 s (Yao et al., 2006; Liang and Langston, 2009b; Li et al., 2010a, 2010b; Yang et al., 2011), whereas teleseismic surface waves are more stable for

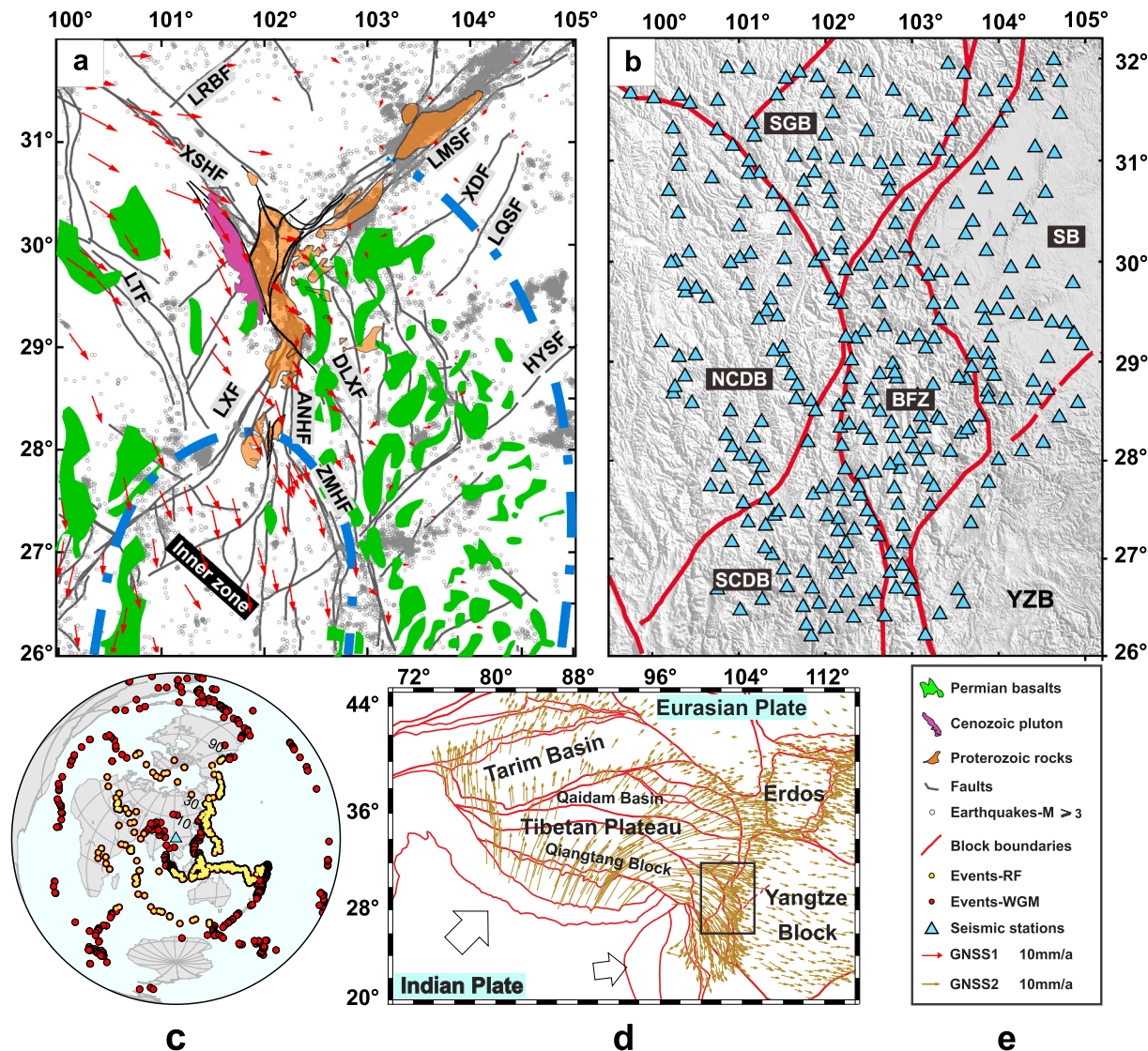


Fig. 1. (a) Geological setting. Purple, brown and green shadows represent Cenozoic pluton, Proterozoic rocks, and Permian flood basalts of Emeishan large igneous province, respectively (Burchfiel et al., 1995; Wang et al., 2013b); the red arrows are the GNSS (Global Navigation Satellite System) velocity relative to the stable Yangtze block (Zhang, 2008); gray circles are the earthquakes with magnitude of $M \geq 3$ from 2009 to 2019 (Long et al., 2020; collected from China Seismic Experimental Site); the gray lines are the faults (Deng et al., 2003) — ANHF: Anning He Fault; LMSF: Longmenshan Fault; XSHF: Xianshuihe Fault; LXF: Lijiang-Xiaojin Fault; LTF: Litang fault; LRBF: Longriba Fault; XDF: Xinjing-Deyang Fault; LQSF: Longquanshan Fault; HYSF: Huayingshan Fault; ZMHF: Zemuhe Fault; DLSF: Daliangshan Fault. (b) The distribution of Temporary West Sichuan Array (TWSA, light blue triangles) and block boundary (Red lines). BFZ: Block boundary fault zone; SGB: Songpan-Ganzi Block; SB: Sichuan Basin; YZB: Yangtze Block; SCDB: south Chuandian Block; NCDB: north Chuandian Block. (c) Earthquakes used in this work, where the red dots and the yellow dots represent the epicenter of the earthquakes applied to the WGM and RF, respectively. (d) The horizontal GNSS velocity relative to the stable Eurasian block (Zhao et al., 2015), the black orthogon represents the study area in this work. (e) Legends of subfigures a–c. (For interpretation of the references to colour in this figure legend, the reader is referred to the web version of this article.)

periods ranging from 25 s to 100 s or longer (depending on the corner frequency of the instrument). Therefore, the teleseismic waveform has better constraint on the upper mantle (Yao et al., 2010; Yang et al., 2011).

RFs are sensitive to elasticity contrasts and are usually used to study the interfaces of Moho, 410 km and 660 km (Langston, 1977; Ligorría and Ammon, 1999; Zhu and Kanamori, 2000), or crustal Poisson's ratio (He et al., 2017; Chen et al., 2021). The difference in arrival times in the two orthogonal phases of shear waves can reveal the average anisotropy of the crust or the whole lithosphere (Silver and Chan, 1991; Chang et al., 2017; Gao et al., 2018; Yang et al., 2022). Crustal azimuth anisotropy can be derived from the azimuth-dependent arrival time of the P-to-S conversions from the Moho (Liu and Niu, 2012; Kong et al., 2016; Zheng et al., 2018). Compared to surface wave tomography, RF has a higher horizontal resolution but a weak vertical resolution.

Joint inversion using multiple seismic datasets can provide additional details and constraints for the model. For example, the joint inversion of RFs and surface wave DCs can improve both the vertical and horizontal resolutions of a 3D Vs model (Julià et al., 2000; Herrmann and Ammon, 2002, 2004; Liu et al., 2014; Liu et al., 2018) while the joint inversion of Rayleigh wave dispersion curves and the amplitude ratio between vertical and radial components (ZH ratio) of Rayleigh waves can help to better constrain the velocity model in shallower (Chong et al., 2015; Tanimoto and Rivera, 2008). The combination of Rayleigh wave dispersion curves obtained from ambient noise cross correlations and teleseism waveforms was utilized to invert a wider depth range 3D Vs model (Bodin et al., 2012.; Yang et al., 2011; Porter et al., 2016). The joint inversion of body waves and surface wave DCs can be used to improve both the vertical and horizontal resolutions of anisotropic structure and seismic velocity model (Bodin et al., 2016; Marone and Romanowicz, 2007; Yuan and Romanowicz, 2010; Yuan et al., 2011).

In this study, we combined azimuth-dependent Rayleigh wave DCs and RFs to jointly invert the 3D Vs model and azimuthal anisotropy structure of the southeastern Tibetan Plateau. Rayleigh wave DCs in the period ranges of 5–20 s and 21–60 s were calculated using ambient noise tomography (ANT) (Shapiro and Campillo, 2004; Yao et al., 2006; Liang and Langston, 2009b) and the WGM (Liang and Langston, 2009a; Maeda et al., 2016; Zhou et al., 2017; Cao et al., 2020b), respectively. The azimuth-dependent RF is calculated using the individual Iterative Time-Domain Deconvolution method (Ligorría and Ammon, 1999). In the 3D model inversion step, the Azimuth-Dependent Dispersion Curve Inversion method (ADDCI, Liang et al., 2020) is applied with the azimuth-dependent RFs for joint inversion of 3D Vs model and the azimuthal anisotropy structure. Using three types of seismic data for joint inversion, our model should have a better constraint on the isotropic and anisotropic structure of the southeastern Tibetan Plateau lithosphere.

2. Data and methods

2.1. Methods

The methodologies of ANT (Yao et al., 2006; Liang and Langston, 2009b; Li et al., 2010a; Yang et al., 2011) and RF (Langston, 1977; Ligorría and Ammon, 1999; Zhu and Kanamori, 2000) are well known. In this section, we introduce the basic theory of WGM and joint inversion involving the three methods.

2.1.1. The wave gradiometry method

The WGM is a data processing technique for seismic dense arrays (Langston, 2007a, 2007b, 2007c; Liang and Langston, 2009a), and is suitable for analyzing body waves (Sollberger et al., 2016; Langston and Ayele, 2016), surface waves (Liang and Langston, 2009a; Liu and Holt, 2015; Zhou et al., 2017; Cao et al., 2020b; Chang et al., 2022), and ambient noise (Cao et al., 2020a; De Ridder and Curtis, 2017). In a small-scale region, the physical properties of the medium vary slowly,

and the wave gradient may be given by Langston (2007c):

$$\frac{\partial u}{\partial i} = A_i u + B_i \frac{\partial u}{\partial t}, i = x, y \quad (1)$$

where, $\partial u / \partial i$ and $\partial u / \partial t$ are the space and time derivatives of u , A_i and B_i represent the normalized change in amplitude and wave slowness, respectively. The wave propagation parameters are given by Langston (2007c).

$$c = \left(B_x^2 + B_y^2 \right)^{-\frac{1}{2}}, \quad (2)$$

$$\Theta = \tan^{-1} \frac{B_x}{B_y}, \quad (3)$$

$$A_r = A_x \sin(\Theta) + A_y \cos(\Theta), \quad (4)$$

$$A_\Theta = r (A_x \cos(\Theta) - A_y \sin(\Theta)), \quad (5)$$

where, c , Θ , A_r , and A_Θ represent the phase velocity, azimuth, geometrical spreading, and radiation pattern, respectively; r is the epicentral distance between the earthquake and reference location $[x_0, y_0]$ (red dot in Fig. S1).

A reducing velocity method (Langston, 2007a) and a weighted inversion method (Liang and Langston, 2009a) are used to solve the wave spatial gradients $[\partial u / \partial x, \partial u / \partial y]$. At time t , the observed waveform $[u_1^{obs}, u_2^{obs}, \dots, u_N^{obs}]^T$ in the supporting stations (black triangles in Fig. S1) can be related to a matrix of first-order approximations of the Taylor series (Liang and Langston, 2009a; Maeda et al., 2016).

$$w u^{obs} = w G m$$

$$\begin{aligned} \mathbf{u}^{obs} &= \begin{bmatrix} u_1^{obs}(x_1, y_1; t) \\ u_2^{obs}(x_2, y_2; t) \\ \vdots \\ u_N^{obs}(x_N, y_N; t) \end{bmatrix} \\ \mathbf{G} &= \begin{bmatrix} 1 & \frac{\partial x_1}{\partial x} & \frac{\partial y_1}{\partial x} \\ 1 & \frac{\partial x_2}{\partial x} & \frac{\partial y_2}{\partial x} \\ \vdots & \vdots & \vdots \\ 1 & \frac{\partial x_N}{\partial x} & \frac{\partial y_N}{\partial x} \end{bmatrix} \\ \mathbf{m} &= \begin{bmatrix} u_0 \\ \frac{\partial u}{\partial x} \\ \frac{\partial u}{\partial y} \end{bmatrix} \\ \mathbf{w} &= \begin{bmatrix} w_1 & & & \\ & w_2 & & \\ & & \ddots & \\ & & & w_N \end{bmatrix} \end{aligned} \quad (6)$$

where, subscript N represents the number of supporting stations; $\partial x_j = x_j - x_0$; $\partial y_j = y_j - y_0, j = 1, 2, \dots, N$; w_j is the weighting factor associated with a higher-order truncation error (Liang and Langston, 2009a); u_0 and $[\partial u / \partial x, \partial u / \partial y]$ are the waveform and wave gradients, respectively, in the reference location $[x_0, y_0]$ at time of t . We need more than three supporting stations to solve wave gradients and u_0 is reconstructed at the same time (Maeda et al., 2016). The reducing velocity method can suppress the higher-order truncation error from the phase velocity (Langston, 2007a; Liang and Langston, 2009a). Using the method proposed by Liang and Langston (2009a), we obtained the wave propagation parameters beneath the reference locations (eq. 2–5).

All parameters produced by eqs. (2)–(5) are time series. We consider the values at the time of the envelope peak of the Rayleigh wave as the final parameter (Liang and Langston, 2009a). Looping for earthquakes

in different back azimuths, we can obtain the azimuth-dependent Rayleigh wave phase velocity $c(\theta)$ and the associated back azimuths θ . The azimuthal anisotropy of Rayleigh waves can be obtained by fitting the $c(\theta)$ (Backus, 1965; Smith and Dahlen, 1975):

$$c(\theta) = c_0 + a_R \cos(2\theta) + b_R \sin(2\theta), \quad (7)$$

where, c_0 represents the isotropic phase velocity of the Rayleigh wave; a_R and b_R are anisotropic parameters. The magnitude of anisotropy (MOA) and fast propagation direction (FPD) are given by:

$$\gamma_R = 2 \times \sqrt{a_R^2 + b_R^2} / c_0 \approx (\max(c) - \min(c)) / c_0, \quad (8)$$

$$\phi_R = \frac{1}{2} \arctan\left(\frac{b_R}{a_R}\right), \quad (9)$$

where, γ_R and ϕ_R represent the MOA and FPD, respectively.

2.1.2. The Azimuth-dependent joint inversion method

The ADDCI method inverts the azimuthal anisotropy of shear waves directly by independently inverting the dispersion curves that vary with back azimuths (Liang et al., 2020). Thus, it provides a workable way to combine azimuth-dependent RFs and azimuth-dependent dispersion curves to jointly invert 3D Vs and anisotropy. The results from the joint inversion of surface wave dispersion curves and RFs/body waves have a better constraint on the velocity or anisotropy variation (Herrmann and Ammon, 2004; Liu et al., 2014; Liu et al., 2018; Bodin et al., 2016).

An azimuth-dependent joint inversion (ADJI) method is proposed in this study. The ADJI method inherits the basic idea of the ADDCI method (Liang et al., 2020) to invert 3D anisotropy and takes advantage of the different sensitivities of the WG, ANT, and RF. This new method is an improvement to our previous work on WGM (Liang and Langston, 2009a; Cao et al., 2020b) and the ADDCI method (Liang et al., 2020).

Similar to the ADDCI method, once the azimuth-dependent Vs model is obtained, the 3D azimuthal anisotropy can be determined by (Crampin, 1984; Liang et al., 2020):

$$v_{sv}(\theta) = \frac{1}{p} \left(1 - \frac{a_{sv}}{p} \cos(2\theta) - \frac{b_{sv}}{p} \sin(2\theta) \right) \quad (10)$$

where, θ is the back azimuth; p represents the isotropic slowness; $1/v_{sv}^{iso}$, a_{sv} , and b_{sv} are anisotropic parameters of the shear wave. We estimated the MOA and FPD of the shear wave using the same method as that used for Rayleigh waves (eqs. 8 and 9).

The arrival times of the PmS phase also shift systematically as a cosine function of the back azimuth in an anisotropic medium (Liu and Niu, 2012; Kong et al., 2016):

$$t = t_0 - \frac{\delta t}{2} \cos[2(\phi_{rf} - \theta)] \quad (11)$$

shifting to

$$t = t_0 \left(1 - \frac{a_{rf}}{t_0} \cos(2\theta) - \frac{b_{rf}}{t_0} \sin(2\theta) \right) \quad (12)$$

where, t and t_0 are the PmS arrival times in the anisotropic and isotropic models, respectively. δt denotes the MOA, and ϕ is FPD. $a_{rf} = \delta t \cos(2\phi_{rf})/2$, $b_{rf} = \delta t \sin(2\phi_{rf})/2$.

As illustrated in Fig. 2, the general process of the ADJI method is as follows:

Step 1: Data collection and pre-processing. Because of the availability of a large amount of data for ANT and WGM, some standards are adopted to automatically process the data. More details in sections 2.2.1 and 2.2.3.

Step 2: Obtain the Rayleigh wave phase velocity and anisotropy, and extract the RFs. ANT and WGM were applied to calculate the phase velocity and anisotropy in short periods and long periods, respectively

(Fig. 2a, b). The RFs were extracted simultaneously (Fig. 2c).

Step 3: Preparation of the DCs and RFs for the joint inversion of azimuth-dependent 1D Vs models. Eq. (7) was used to extract the DCs in every back azimuth bins with an interval of 10° (Fig. 2d). The RFs of the earthquakes in different azimuths were also stacked to the back azimuth bins with an interval of 10° (Fig. 2e). Therefore, a DC and a RF were extracted for every back azimuth bin on a grid point (Fig. 2f).

Step 4: Joint inversion of the dispersion curve and RF. Using the linearized least squares joint inverse method (Julià et al., 2000; Herrmann and Ammon, 2002, 2004) to simultaneously invert the DC and RF for 1D Vs models (Vs as a function of depth) for each back azimuth bin and grid point. Fig. 2g shows the azimuth-dependent 1D Vs models of the k th grid point. If there are N_g grid points and 18 azimuth bins, then the total 1D Vs model is $N_{mld}=18 \times N_g$.

Step 5: Assemble 3D Vs and anisotropy models. Looking at every grid, at each depth, there are 18 velocities that vary with the back azimuths. Using eq. (10) to fit these 18 azimuth-dependent 1D Vs models with back azimuths, we can find the v_{sv}^{iso} , MOA, and FPD at each grid point and depth (Fig. 2h). For more details, refer to Liang et al. (2020).

2.2. Data processing

From October 2006 to July 2009, the temporary West Sichuan array (TWSA) (Fig. 1b) with approximately 303 CMG-3ESPC (60 s / 50 Hz) wide-band seismographs was deployed in the southeastern Tibetan Plateau by the Institute of Geophysics, China Earthquake Administration (ChinArray, 2006). The TWSA dataset has been applied to the ANT method (Liu et al., 2014; Li et al., 2010a), receiver function analysis (Zheng et al., 2018; Chen et al., 2021), focal mechanism solution (Liu et al., 2009), SKS splitting (Yang et al., 2018), P-wave tomography (Guo et al., 2009), the WGM (Cao et al., 2020b) and eikonal tomography (Wang et al., 2020). Here, the ANT method, WGM, and receiver function were applied together to the TWSA for the joint inversion of the 3D Vs model and 3D azimuthal anisotropy structure.

2.2.1. Data processing for ANT

We applied the one-bit method to calculate the daily cross-correlation functions (CCFs) of the TWSA (Yao et al., 2006; Cupillard et al., 2011). For each station pair, the daily cross correlations from October 2006 to July 2009 were stacked into one CCF (Fig. S2), and the Rayleigh wave DCs in periods from 5 to 30 s were calculated using the CCF Analysis Dispersion Technique developed by Yao et al. (2006).

The signal-noise ratio (SNR) of CCF is expressed as

$$\text{SNR} = A_{\text{max}} / A_{\text{mean}} \quad (13)$$

where, A_{max} and A_{mean} are the maximum and mean amplitude of the CCF envelope, respectively. We automatically discarded the dispersion points adopting the following standards: (1) SNR of associate CCF < 5 , (2) the distance of station pair < 3 wavelengths, and (3) dispersion points diverge 0.15 km/s from the trend of dispersions from similar raypath (Fig. S3a). Abnormal dispersion points that cannot be eliminated by the above automatic programs are carefully inspected manually. Finally, we obtained 10,000–30,000 rays for periods ranging from 5 s to 30 s (Fig. S3b). The dispersion and anisotropy maps with a grid size of $0.15^\circ \times 0.15^\circ$ were inverted using the technique described by Liang et al. (2004, 2020); the regularization parameters for velocity and anisotropy were both 0.2.

A checkerboard test was applied to analyze the resolution of the ANT method on the TWSA, in which the velocity anomaly, the MOA, and the checkerboard size were set to ± 0.35 km/s, 8% and $0.45^\circ \times 0.45^\circ$, respectively. The results of the checkerboard test can resolve the general patterns of both velocity and anisotropy (Fig. 3).

2.2.2. Data processing for receiver function

Three steps are taken to process RFs:

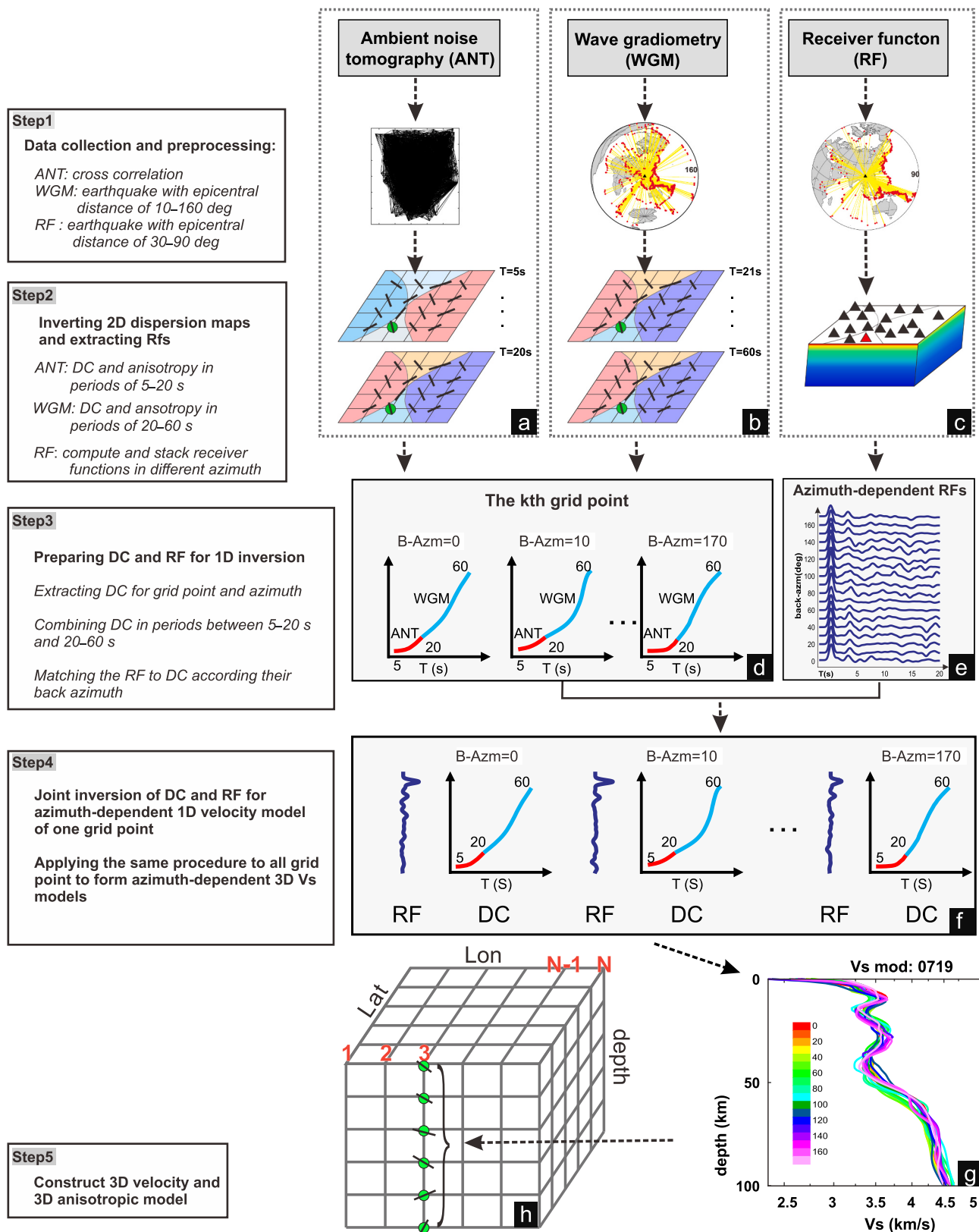


Fig. 2. Flow chart for Azimuth-Dependent Joint Inversion method. (a) Ambient noise tomography for dispersion curves in periods of 5–20 s. Black lines are raypaths; colour base maps represent phase velocities; black bars represent anisotropies; two green dots represent the kth grid point in periods of 5 s and 20 s. (b) WGM for dispersion curves in periods of 21–60 s. (c) Calculation of RF. The red triangle represents the station neaby the kth grid point. (d) The combined dispersion curves in different back azimuth; red and light blue curves represent the dispesion curves obtained by ANT and WGM, respectively. B-Azm: back azimuth. (e) The stacked RFs of the red station in different azimuth bins. (f) RF-DC pairs in different backazimuth bins. DC = dispersion curve. (g) azimuth-dependent 1D Vs models in the kth grid point, colour bar marks the backazimuth in different colour. (h) 3D Vs model and anisotropic structure. Green dots mark the results of kth grid point in different depth. (For interpretation of the references to colour in this figure legend, the reader is referred to the web version of this article.)

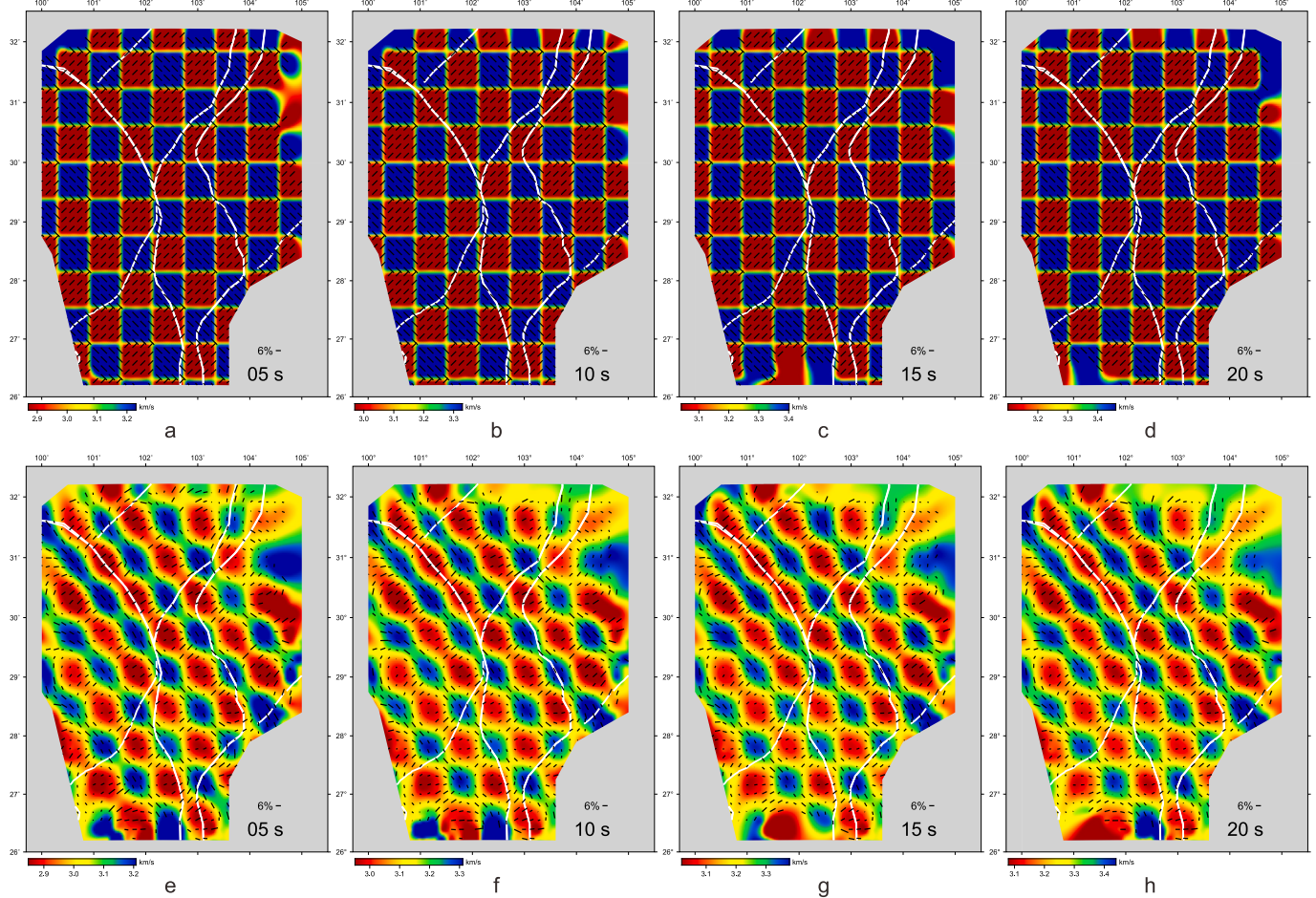


Fig. 3. Checkerboard test for the ambient noise tomography.

(1) The Iterative Time-Domain Deconvolution method developed by [Ligorria and Ammon \(1999\)](#) was used to compute the RFs in this study. Using a total of 808 earthquakes ($M_s \geq 5.5$) within an epicentral distance between 30° and 90° recorded by the TWSA (yellow dots in Fig. 1c), we obtain 4800 RFs with a Gaussian factor of 2.0.

(2) The RFs were corrected to a uniform ray parameter of 0.065 ([Zhu and Kanamori, 2000](#))

(3) The RFs are stacked in the back azimuth bins with an interval of 10° . In addition, according to the anisotropy model of PmS phase arrival time (eq. 12; [Kong et al., 2016](#)), the back azimuths of RFs $>180^\circ$ were subtracted by 180° to improve the backazimuth coverage.

2.2.3. Data processing for wave gradiometry method

The waveforms of 1316 earthquakes with $M_s \geq 5.5$ and epicentral distances ranging between 5° – 160° (red dots in Fig. 1c) were applied to the WGM. The bad waveforms were automatically discarded according to the SNR and arrival time of the Rayleigh wave train. The technical details are as follows:

- (1) Cutting waveforms with a time window of 60 s before and 3600 s after the P-wave arrival.
- (2) The waveforms were filtered with a frequency band of $1/(CT + 0.1CT)$ and $1/(CT - 0.1CT)$, where CT is the center period.
- (3) It is assumed that the Rayleigh wave energy is strongest in the vertical component. Its apparent group velocity is given by:

$$V_i^* = \frac{D_i}{T_i} \quad (14)$$

where, subscript i denotes the i th station; D_i is the epicentral distance;

and T_i (blue points in Figs. 4a, 4b) is the arrival time of the maximum amplitude of the envelope in the time window W_i from $D_i/5(\text{km/s})$ to $D_i/2(\text{km/s})$ (yellow shadow in Fig. 4b). Waveforms with V_i^* 0.1 km/s greater or smaller than the median apparent group velocity (V_{mi}^*) were discarded (black circles in Fig. 4c).

(4) The SNR of Rayleigh wave is given by

$$\text{SNR} = \frac{A_S}{A_N} \quad (15)$$

where, A_S is the amplitude of the envelope at T_i ; A_N is the mean amplitude of the envelope in the time window from $T_i + 5^*\text{CT}$ to 3600 s after P-wave arrival (red envelope in Fig. 4a). Waveforms with an SNR lower than 5 were discarded.

(5) The waveforms in which amplitudes at T_i are approximately 30% larger or smaller than surrounding stations are also discarded ([Liang and Langston, 2009a](#)).

The automatically selected and discarded waveforms are shown in Fig. 5a and b, respectively. The chosen waveforms were regarded as good-quality data and were applied to the WGM. Fig. S4 shows the number of earthquakes used in different periods.

When combining the DCs obtained by the ANT method and the WGM in space, the locations of grid points used in the ANT method were used as reference locations in the WGM. Fig. 6 shows the WG analysis results for one grid point. The wave fields of the Nevel'sk M5.5 earthquake (UTC:2007-08-02 10:37:31) propagated from the northeast direction

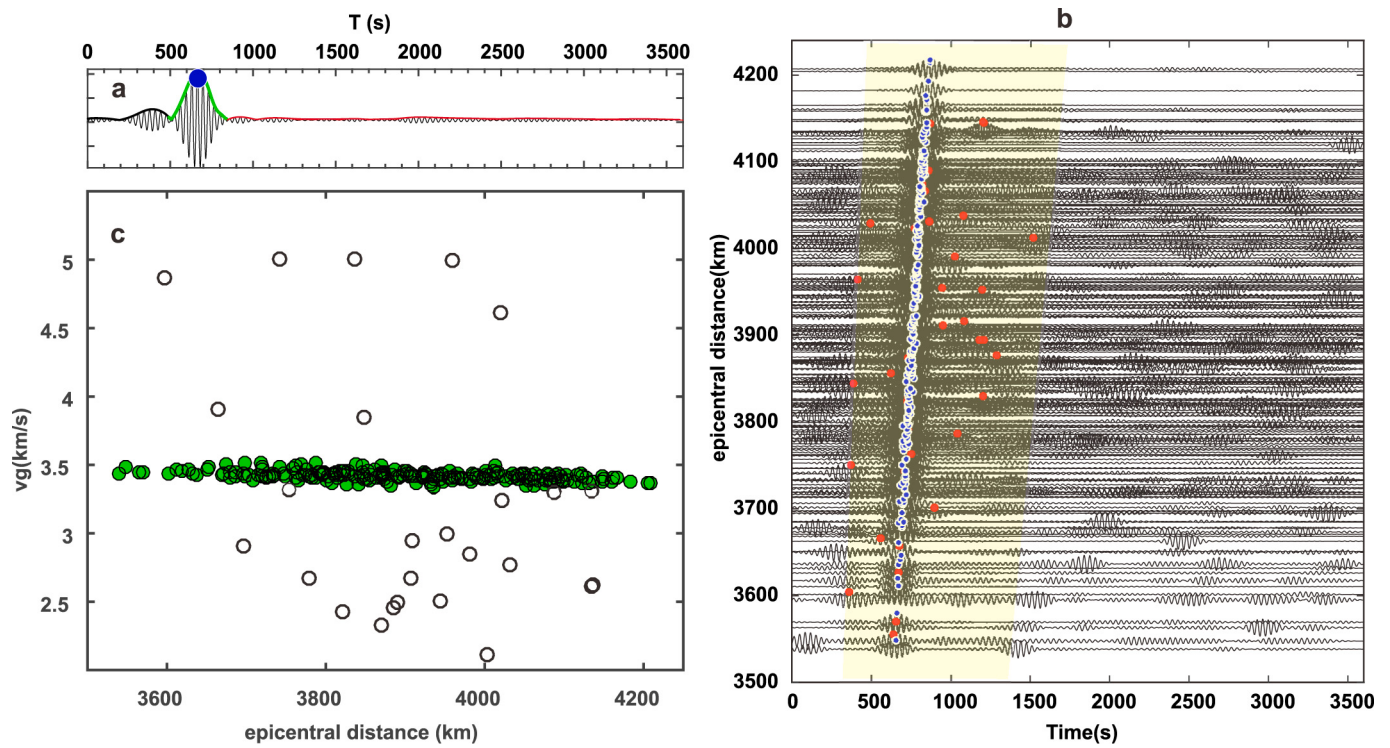


Fig. 4. Automatically selecting for waveforms of Nevel'sk M5.5 earthquake (UTC: 2007-08-02 10:37:31). (a) The telesismic waveform of one station with center period of 35 s. The blue dot marks the arrival time of the maximum amplitude of the envelope in the time window of W_i (yellow shadow in Fig. 3b), the signal of Rayleigh wave is marked by green envelope, and the red envelope in the right side of Rayleigh wave is defined as noise for calculating the signal-noise ratio (SNR); (b) waveforms of Nevel'sk M5.5 earthquake (UTC: 2007-08-02 10:37:31), the blue (good-quality waveforms) and the red dots (waveforms with low SNR, aberrant V_i^* and amplitudes at T_i are about 30% larger or smaller than surrounding stations) mark the arrival time of maximum amplitude; (c) V_i^* distribution with epicentral distance, the green points and the black circles are the V_i^* inside and outside the range of $V_{mi}^* \pm 0.1$ km/s.

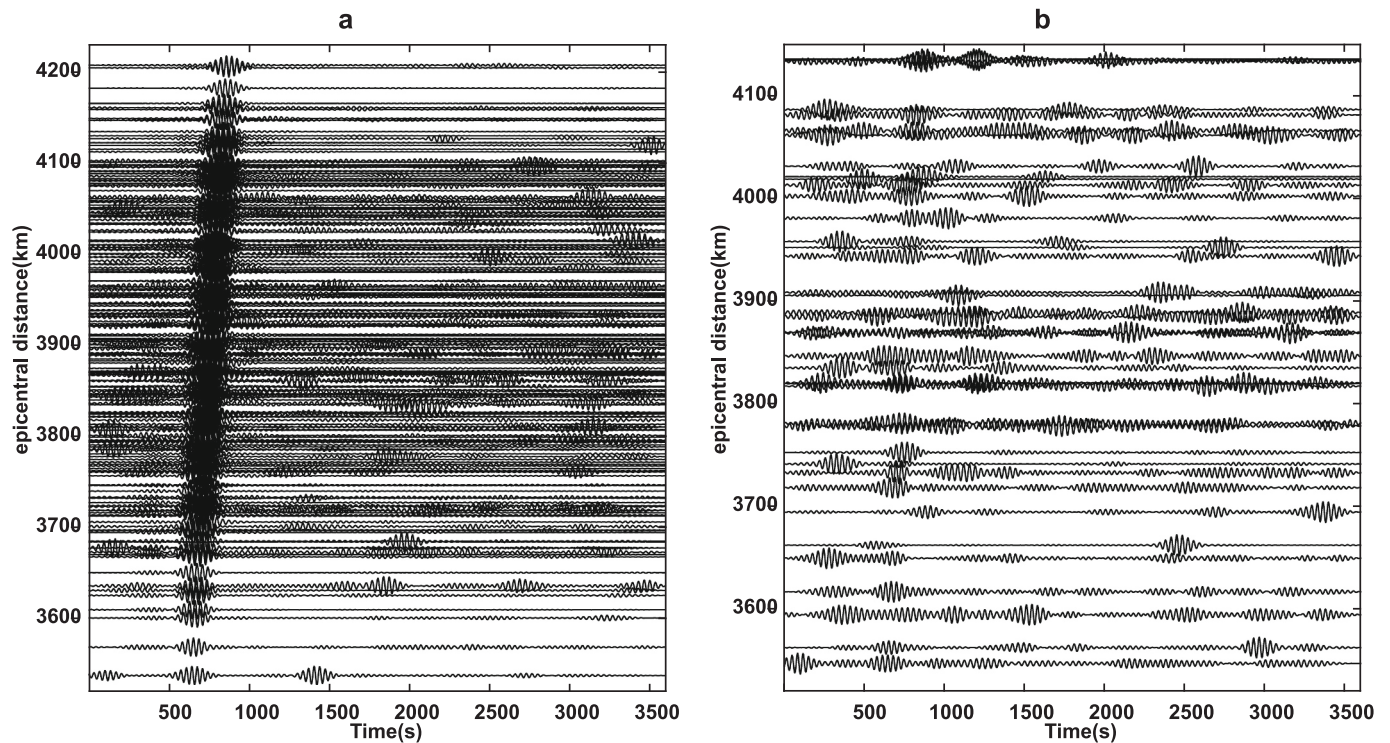


Fig. 5. The good-quality waveforms (a) and the discarded waveforms (b) of the Nevel'sk M5.5 earthquake (UTC: 2007-08-02 10:37:31). The central period is 35 s.

(blue line in Fig. 6a). The waveforms recorded by the supporting stations

were used to calculate the wave gradient (eq. 6), and the additional

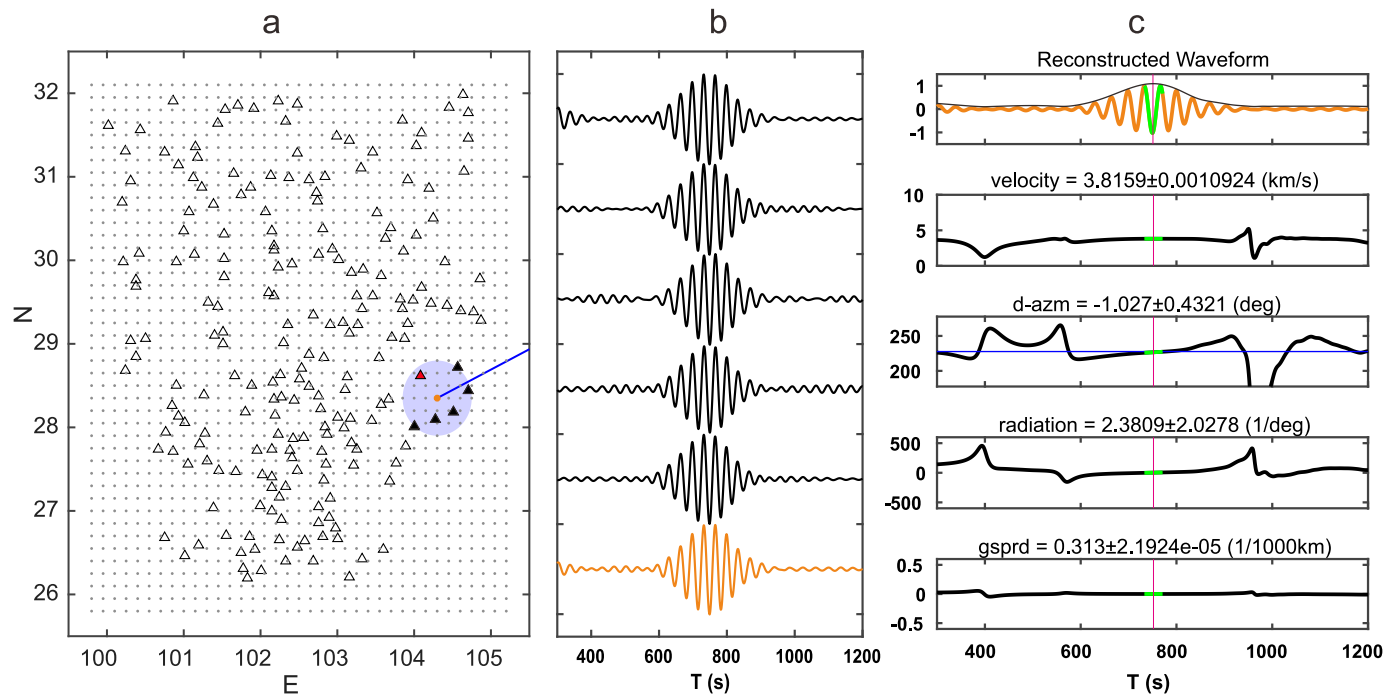


Fig. 6. The wave gradiometry analysis of a grid point. (a) Geometry of a subarray centered at the brown grid point. Gray dots mark the meshing grid points; brown dot is the reference point at which the WG analysis is applied, shadow area is the range of a subarray, triangles are the stations of the Temporary West Sichuan array (TWSA), where the black solid triangles represent supporting stations with good-quality waveforms, and the red solid triangles are the supporting station with bad-quality waveform; blue line is the raypath of the Nevel'sk M5.5 earthquake (UTC: 2007-08-02 10:37:31). (b) Waveforms of the Subarray. The brown waveform is the reconstructed waveform on the reference grid point (t_0 in eq. 6), black waveforms are the waveforms of the supporting stations. (c) Time-series results of wave propagation parameters on the reference location; subfigures from top to bottom are the reconstructed waveform, phase velocity, azimuth variation (d-azm), radiation pattern, and the geometric spreading (gsprd) beneath the reference location, respectively. The horizontal blue line is the great circle back azimuth, the vertical purple lines mark the timing of the waveform peak, and the results in time series of one period in green range are used for estimating standard deviation. (For interpretation of the references to colour in this figure legend, the reader is referred to the web version of this article.)

waveform at the reference location (brown waveform in Fig. 6b, c) was also reconstructed simultaneously. Fig. 6c shows that the wave propagation parameters beneath the reference location were stable in the time window of the Rayleigh wave. Looping for all reference locations (gray dots in Fig. 6a), we obtained the wave propagation parameters of one earthquake in the entire study area. Looping for earthquakes in different back azimuths and periods of 20–60 s, we can obtain the phase velocity varying with back azimuth in this period range. The isotropic phase velocity maps and azimuthal anisotropy pattern of Rayleigh waves are generated by fitting the azimuth-dependent phase velocities with the anisotropic function of Rayleigh waves (eq. 7; Cao et al., 2020b).

In contrast to the ANT method, where the resolution depends on the density of the raypath, the resolution of the WGM is based on the density of the seismic array. Here, we take a series of synthetic tests to estimate the effects of the radii of the subarray and smoothing parameter, wavelength, and noise level on the resolution of the WGM. The wave function is expressed as a Gaussian function:

$$u(t, r) = \frac{1}{r} \exp \left[-\alpha \left(t - r \left(\frac{1}{v_0 + a \cos(2\theta) + b \sin(2\theta)} \right) \right)^2 \right] (1 + N). \quad (16)$$

where, r is the epicentral distance; v_0 is the isotropic velocity; a and b are anisotropy parameters; θ is the back azimuth; and N is the random noise. As shown in Fig. 7, the Gaussian wave propagated across an 18×11 array with a uniform spacing of 26 km (white dots in Fig. 7a–7c), which is close to the average station spacing of the TWSA. Reference locations were set to a 35×22 grid matrix with a uniform spacing of 13 km (black bars in Fig. 7a–7c). The distances between the central station and the 17 sources were all set to 100° and the back azimuths varied from 100° to 270° (Fig. 7d).

Based on different periods, the width of the low-velocity belt, random noise, radii of subarray, and smoothing, 11 input models (Table S1) were used to estimate the resolution of WG. Three low-velocity belts with widths of 26, 39, and 52 km (red shaded area in Fig. 7a–7c) were used to test the resolution of the WGM. In these three low-velocity belts, the anisotropy parameters $[a, b]$ of eq. (16) were both set to $[-0.01, 0]$ for synthetic waveforms of different models (Table S1), and v_0 in periods of 20 s and 60 s were set to 3.3 km/s and 3.6 km/s, respectively. In the background medium, the anisotropy parameters $[a, b]$ were both set to $[0.01, 0]$, and v_0 in periods of 20 s and 60 s were set to 3.6 km/s and 3.8 km/s, respectively.

From Mod1 to Mod8, the radii of the subarray and smooth were all set to 0.5° , with the same radii used for the real processing of the TWSA. From Mod9 to Mod11, the radii of the subarrays were set to 0.3° , 0.3° , and 0.5° , respectively, and the radii of smoothing were set to 0.5° , 0.5° , and 0.25° , respectively. While generating the synthetic Gaussian waves, except for Mod7 and Mod8, which were added with 5% and 10% random noise, respectively, the other nine models had no random noise (Table S1).

The recovered phase velocity and azimuthal anisotropy for models Mod1–Mod6 are shown in Fig. 7e, f, g, i, j, and k, respectively. If the subarray radius and smoothing radius are both twice the station spacing (0.5°), the WGM can roughly recover the velocity anomaly with the same scale as the station spacing (Fig. 7e, i). However, the recovery of anisotropy was poor. For an anomaly with a scale of 1.5 times the station spacing, both the velocity and anisotropy can be roughly recovered (Fig. 7f, j) while for an anomaly with a scale of twice the station spacing, both can be recovered with little errors (Fig. 7g and k). Wavelength has little effect on resolution in the WGM, but the premise is that the station spacing and the period of Rayleigh waves need to meet a sufficiently small truncation error (Langston, 2007c; Liang and Langston, 2009a).

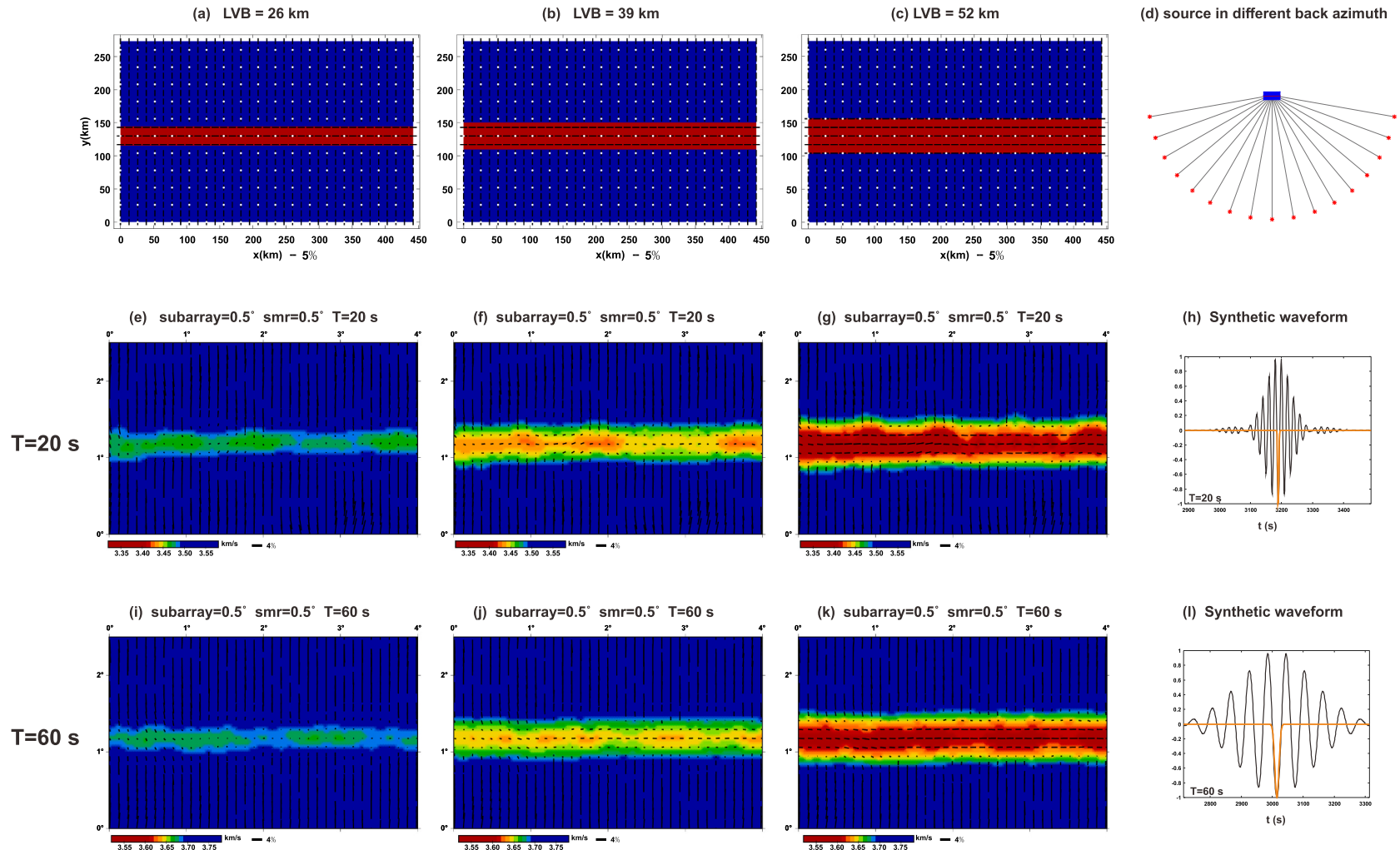


Fig. 7. Rayleigh wave velocities and azimuthal anisotropies determined from wave gradiometry numerical experiment. (a)–(c) Diagrams for input models with 26 km, 39 km, and 52 km wide low velocity belt (LVB) (red shaded area); blue shaded areas are the background medium; direction and length of black bars represent the FPD and MOA; white dots are seismic array with station spacing of 26×26 km, the locations of black bars represent reference locations with spacing size of 13×13 km. FPD: fast propagation direction; MOA: magnitude of anisotropy. (d) Distribution of sources (red dots) in different back azimuth. (e)–(g) Phase velocity and azimuthal anisotropy recovered from Mod1–Mod3. (h) Synthetic wave with Gaussian factor of 0.1 (brown curves) and filtered waveform with center period of 20 s (black curves). (i)–(k) Phase velocity and azimuthal anisotropy recovered from Mod4–Mod6. (l) Synthetic wave with Gaussian factor of 0.012 (brown curves) and filtered waveform with center period of 60 s (black curves). (For interpretation of the references to colour in this figure legend, the reader is referred to the web version of this article.)

The recovered models of Mod 7 and Mod 8 show that even though the Gaussian wave contains 5% or 10% random noise, if both the subarray radius and the smoothing radius are twice the station spacing, the WGM can still generally recover the velocity and anisotropy with the same scale as subarray (Fig. S5). The recovered models of Mod9, Mod10, and Mod11 show that a larger subarray radius or smooth factor can reduce the influence of truncation errors on anisotropy, but can also reduce the resolution (Fig. S6).

2.2.4. Joint inversion

Before joint inversion, the Rayleigh wave phase velocity and anisotropy at periods of 5–30 s and 20–60 s were calculated by ANT and WGM, respectively, and the results in the three overlapping periods were compared in Fig. S7. The differences in velocities, MOAs, and FPDs between these two methods are <0.05 km/s, 1.9%, and 25°, respectively, in most regions. Relatively large differences were observed in the margins of the study area. The ANT has poor resolution in the edge area owing to its sparser raypath coverage. However, the resolution or errors of the WGM are based on the subarray radius, smoothing radius, and supporting stations (Langston, 2007a; Liang and Langston, 2009a; section 2.2.3). As the results for grids with less than five supporting stations have been discarded, we are more confident in the results obtained by the WGM in the margin of the study area in these three overlapping periods. In addition, the comparison at a period of 30 s shows a larger velocity difference compared to that at a period of 20 s. Considering that the surface wave energy from ambient noise cross-correlation is weak over long periods, we only use the DC calculated by ANT in the period range of 5 s to 20 s (red curves in Fig. 2d), whereas the DC of 21 s to 60 s is obtained by the WGM using earthquake surface waves (blue curves in Fig. 2d). For each grid and back azimuth, applying the isotropic phase velocities and anisotropies to eq. (7)–(9), we can extract the DCs for the back azimuths of 0–170° with an interval of 10°.

The stacked azimuth-dependent RFs are matched to the azimuth-dependent DCs according to their back azimuths and locations (RFs <0.5° away from the location of the DCs). During the joint inversion of the 1D Vs model, the RF and DCs were assigned the same weighting factor of 0.5. Vp was updated using the Vp/Vs ratio of the initial model. The starting model consisted of 35 layers with an interval of 2 km, 15 layers with an interval of 5 km, and five layers with an interval of 10 km. Each layer had the same Vs of 3.5 km/s.

The 1D Vs model for an individual back-azimuth bin was jointly inverted by an RF and a DC. Fig. 8 shows an example of joint inversion for the azimuth-dependent 1D Vs model at an individual grid point. Additional examples of different grid points are shown in Supporting

Figs. S8–S11. The azimuth-dependent velocities at a depth and a grid point are applied to the anisotropic function of shear waves (eq. 10) to find the anisotropic model and isotropic Vs. The 3D Vs model and the 3D anisotropic structure of the southeastern Tibetan Plateau are constructed by the isotropic Vs and anisotropic results of all grid points at all depths.

3. Results

3.1. The phase velocity and anisotropy of Rayleigh wave

The resolution of the ANT and WGM was tested using the checkerboard test (Section 2.2.1) and the synthetic Gaussian wave (Section 2.2.3), respectively. The standard deviations of Rayleigh wave phase velocities, MOAs, and FPDs estimated by the bootstrap method (Efron, 1979) were mostly <0.05 km/s, 1%, and 20°, respectively (Fig. 9). The standard deviation of the FPDs calculated by WGM was larger than that calculated by ANT, especially for longer periods. First, the azimuth coverage of the raypath used in the ANT was greater than that of the teleseismic raypath used in the WGM. Second, the Rayleigh wave at a frequency of 55–60 s was closer to the cutoff frequency of the TWSA seismograph (Liu et al., 2009).

The phase velocity and azimuthal anisotropy for the six periods are shown in Fig. 10. The fundamental features are as follows: (1) phase velocities in the Sichuan Basin (SB) show a low anomaly at $T = 5$ s and high anomaly appearing at long periods, which is consistent with the consensus that thick sediments overlay in the SB; (2) the south Chuandian block (SCDB), as the inner zone of ELIP (Fig. 1), shows a relatively high velocity at periods of 5 s, 10 s, 20 s, 25 s, 35 s, and 50 s; (3) a wide distribution of low velocity appears in the plateau area at periods larger than 20 s; (4) the Longmenshan Fault (LMSF), Xianshuilu Fault (XSHF), Longriba Fault (LRBF), and Longquanshan Fault (LQSF) divide the anisotropy into different types according to the FPDs or MOAs.

3.2. 3D Vs model and Azimuthal anisotropic structure

Fig. 11 plots the Vs maps and anisotropy obtained by ADJI method. Generally, beneath the north Chuandian block (NCDB) and Songpan-Ganzi block (SGB), the upper crust shows relatively high velocity, and the mid-lower crust and the upper mantle show a low velocity anomaly. The SB shows a low velocity in shallow crust and shows a high velocity in mid-lower crust and upper mantle. ELIP which is located in SCDB and block boundary fault zone (BFZ) show a relatively high velocity in different depths; our anisotropic model shows a distinct regional feature

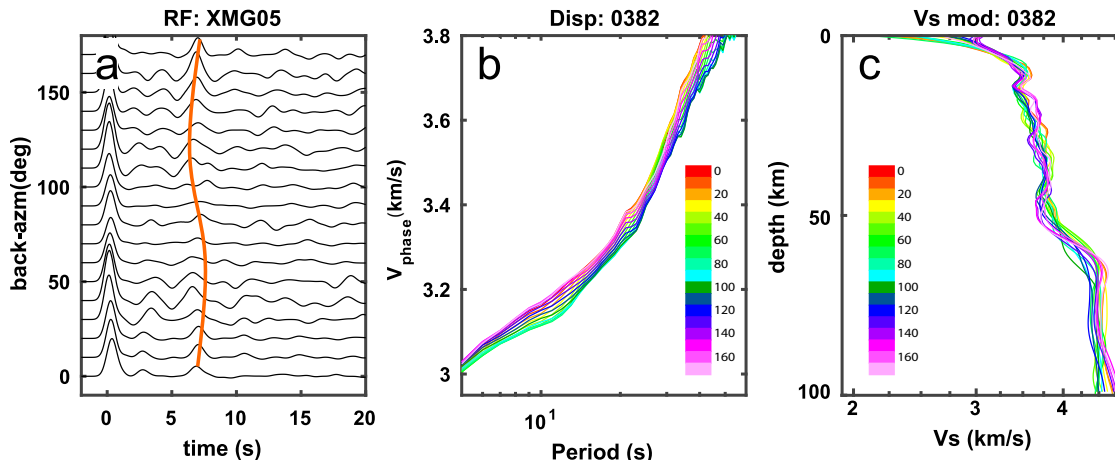


Fig. 8. Joint inversion for one grid point. (a) Azimuth-dependent receiver functions (RFs); brown curve marks the general arrival time of PmS phase. (b) Azimuth-dependent dispersion curves; the colour of dispersion curves present the back azimuth. (c) Azimuth-dependent 1D Vs models. (For interpretation of the references to colour in this figure legend, the reader is referred to the web version of this article.)

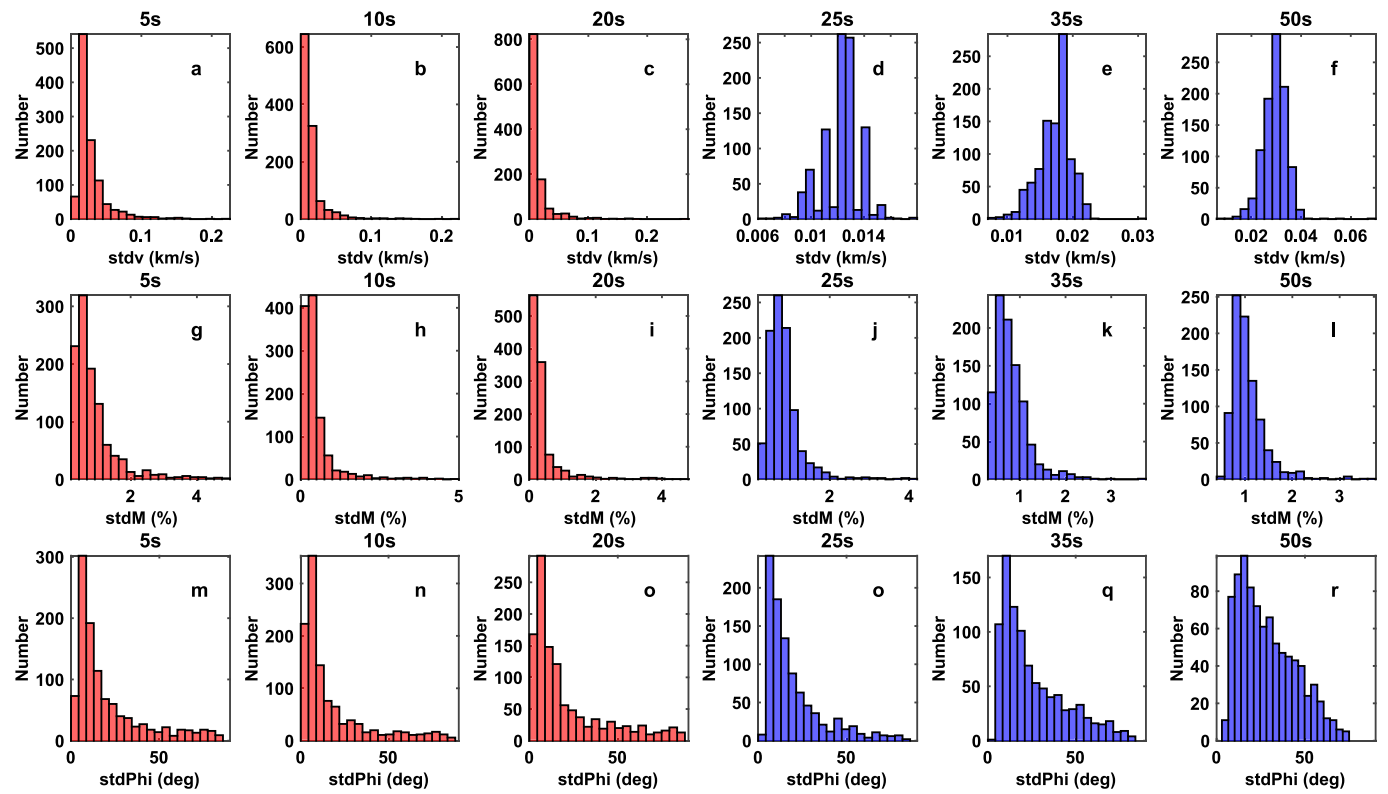


Fig. 9. Histograms for the standard deviations of Rayleigh wave velocity and the azimuthal anisotropy. The red and the blue histograms are the standard deviations from the ambient noise tomography (ANT) and the wave gradiometry method (WGM), respectively. The numbers on the top of histograms are the corresponding periods. stdV, stdM and stdPhi denote the standard deviations of phase velocity, magnitude of anisotropy (MOA), and fast propagation direction (FPD), respectively. (For interpretation of the references to colour in this figure legend, the reader is referred to the web version of this article.)

in the southeastern Tibetan Plateau.

At a depth of 4 km, the distribution of Vs was consistent with the rocks or strata exposed on the surface (Wang et al., 2013b; Geological Bureau of Sichuan Province, 2014). The SB presents a Vs value lower than 3 km/s, where there are thick sediments; The Xichang Basin (28° N, 102.4° E), which is dominated by fluvial and lacustrine red bed facies and filled up to 6 km of Cretaceous sedimentary strata (Xia, 1982; Deng et al., 2018; Burchfiel et al., 1995), shows a low velocity anomaly (~2.9 km/s). In contrast to the SB, the SGB, NCDB, and SCDB experienced uplift and denudation, resulting in rock excavation; thus, they presented as high Vs anomalies. The high velocity in the north of the SGB is associated with the outcrop of the Jurassic monzogranite; the high velocity on the west side of the NCDB and the south end of the Litang Fault (LTF) is associated with the outcrop of Triassic monzogranite (Wang et al., 2013b; Geological Bureau of Sichuan Province, 2014). Effected by fragmenting and/or liquid-filling, XSHF, LXF, LMSF, and ZMHF present relatively low Vs values. FPDs at 4 km depth are basically sub-parallel to the fault strike, such as the LMSF, LQSF, XSHF, Lijiang-Xiaojin Fault (LXF), Anning He Fault (ANHF), and Zemuhe Fault (ZMHF), suggesting the shape-preferred orientation (SPO) of liquid-filled faults (Crampin, 1981). Inside the SB, the LQSF as a boundary separates the anisotropy into two types: on the northwest side of the LQSF, SB shows a weak MOA, whereas in the southeast LQSF, SB shows a stronger MOA. The FPD in the NCDB rotated clockwise along the XSHF and LXF.

Vs and anisotropy at 10 km depth are similar to those at 4 km depth and FPD are mostly sub-parallel to the fault strikes; plateau area (area outside the SB) still shows a relatively high velocity; fault-controlled low velocity zones appear in XSHF and LXF; and FPD in the NCDB rotated clockwise along the XSHF and LXF. In contrast, a high-velocity anomaly of the SB first appears in the south of the LQSF, is consistent with the Weiyuan uplift (Xu, 1997), and low velocity associated with sediment appears on both sides of the LQSF.

At a depth of 20 km, the LMSF and LXF show a clear boundary of the velocity anomaly. The Vs in the SGB and NCDB are mostly lower than 3.5 km/s, and the low Vs anomaly in the internal region of the NCDB is more prominent than that in the SGB. In the SB, SCDB, and BFZ, the Vs value are about 3.6–3.75 km/s, 3.5–3.65 km/s, and 3.45–3.65 km/s, respectively; the high velocity anomaly of SB extends to northwest side of the LMSF into the SGB.

At the depth of 40 km, the distribution of Vs value is also controlled by the major fault zones; in the SB, BFZ, SCDB, SGB, and NCDB are 3.85–3.95 km/s, 3.7–3.85 km/s, 3.55–3.75 km/s, 3.55–3.65 km/s, and 3.2–3.6 km/s, respectively. The low-velocity zones in the SGB and NCDB were restricted by the LMSF, LRBF, XSHF, and LXF. The NCDB still showed a more prominent low Vs value than the SGB. The BFZ exhibits a higher velocity than the SCDB. For the anisotropy at 40 km depth, the FPD gradually changed from NW–SE in the SGB to NE–SW in the LMSF and parallel to the fault strike in the LMSF. The FPD in the margin of the SB rotated around the SB, and LQSF and Huayingshan Fault (HYSF) showed fault-perpendicular and fault-parallel anisotropy.

At a depth of 60 km, the low-velocity zone is distributed mostly along the XSHF, ANHF, and LXF. The high-velocity zone crosses the basin boundary and appears in the northern part of the LMSF and the southeast area of the BFZ. For anisotropy, the FPDs at 60 km depth were similar to those at 40 km depth in most regions. However, FPDs in the Xinjin-Deyang Fault (XDF), LQSF, ANHF, ZMFH, and southern part of the LMSF are perpendicular to the fault strike; MOAs in the southern segment of the XSHF are small.

At a depth of 90 km, low-velocity anomalies are mostly distributed in the LMSF and northeast region of the SGB. Compared to the depths of 40 km and 60 km, the low-velocity anomaly in the NCDB is restricted and mainly distributed to the southwest side of the LTF. SCDB and SB are characterized by high-velocity anomalies, especially SCDB. For the anisotropy, FPD in SCDB is nearly E–W and is dominated by NE–SW

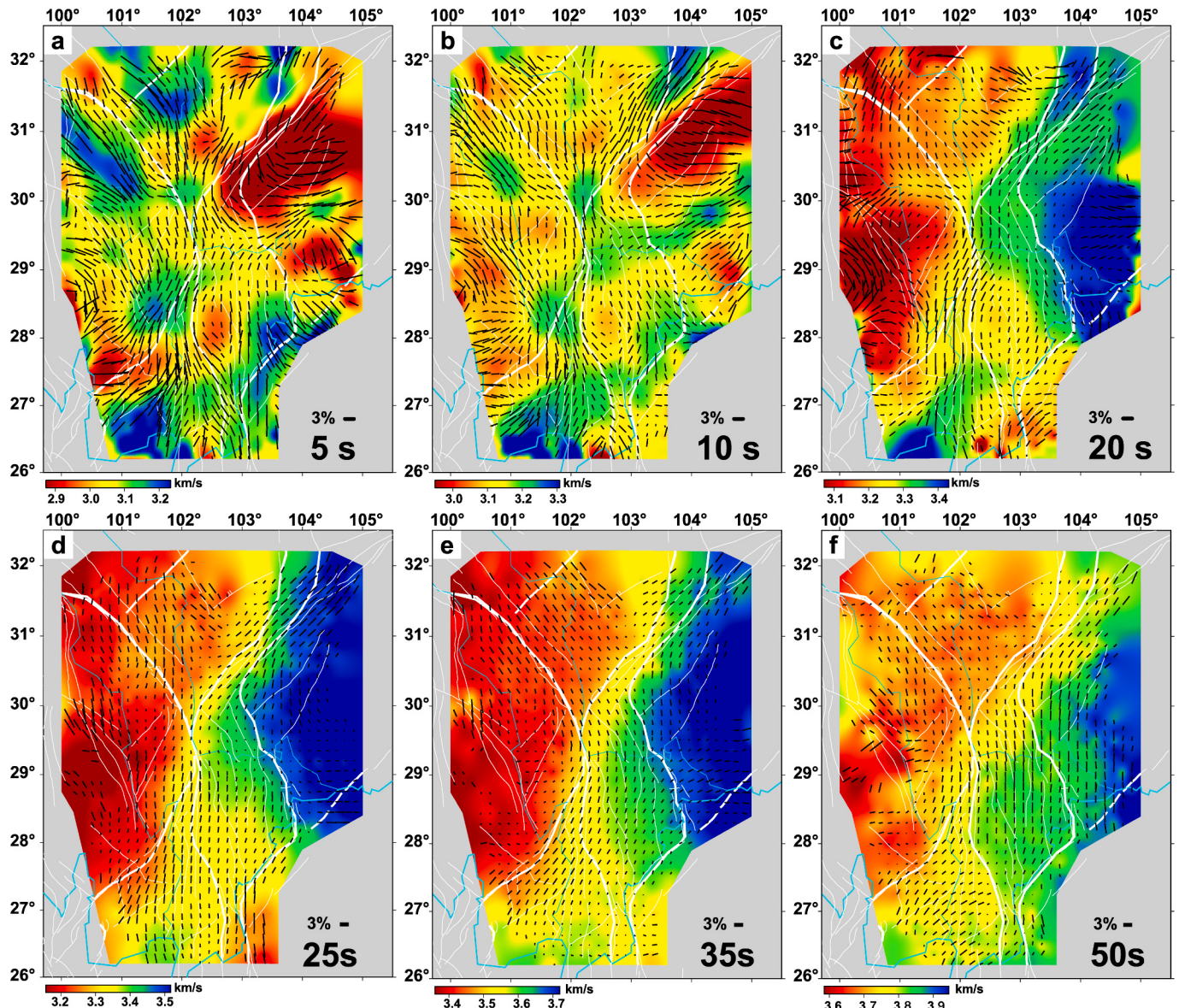


Fig. 10. Phase velocity (base maps) and anisotropy (black bars) obtained by the ambient noise tomography (ANT) (a–c) and wave gradiometry method (WGM) (d–f). Thick and thin white lines are block boundaries and faults, respectively. Light blue lines denote rivers. (For interpretation of the references to colour in this figure legend, the reader is referred to the web version of this article.)

direction in SB; the south segment of XSHF, the north segment of the LMSF, and the LQSF show fault-parallel anisotropy. The BFZ, ANHF, and southern segment of the LMSF show a small MOA.

In Fig. 12, seven profiles of the 3D Vs model provide a good perspective for observing the change in Vs value with different depths in different areas. In profiles AA' (Fig. 12a) and BB' (Fig. 12b), the SB shows a thicker low-Vs layer in the shallow crust; below the LQSF, a high velocity volume is observed in the depth range from 6 km to 20 km; the SB presents as high velocity structure in the mid-lower crust and upper mantle. The velocity change sharply from the SB to the SGB in the mid-lower crust and upper mantle; an obvious low velocity zone (LVZ) with Vs about 3.3–3.5 km/s appears in depth range from 20 km to 35 km beneath the SGB. From the profile CC' to EE' (Fig. 12c–12e), we observe a high velocity volume in the crust and upper mantle of the SCDB and BFZ. In addition, a clear LVZ (3.15–3.5 km/s) is observed in the depth range of 20–40 km beneath the NCDB. A relatively low-velocity zone (3.4–3.5 km/s) appears in the mid-lower crust of the southeast corner of the SCDB, and these two parts are separated by a mushroom-shaped high-velocity volume beneath the SCDB and BFZ (Fig. 12c–12e).

Profiles GG' (Fig. 12g) also show that these two LVZ are not connected with each other while profiles F-F' (Fig. 12f) clearly show that the LVZ in the NCDB is more prominent than that in the SGB.

4. Discussions

4.1. Comparing with other results

Fig. S12 shows the consistent 3D shear wave azimuthal anisotropy between Bao et al. (2020, inverted only by the ambient noise dataset) and this study (ADJI method). Fig. S13 shows the weighted average anisotropy in the depth layers of 1–60 km based on the ADJI method and Bao et al. (2020). The consistency between the two studies was remarkable, with a median angular difference of 17.8°.

In Fig. 13a–13d, the weighted average anisotropy in the depth ranges of 2–20, 20–40, 40–60, and 60–100 km were plotted together with the maximum compressional stress inverted by focal mechanisms in the upper crust (Yang et al., 2018), the crust azimuthal anisotropy derived from the arrival time of the PmS phase (Zheng et al., 2018), and the

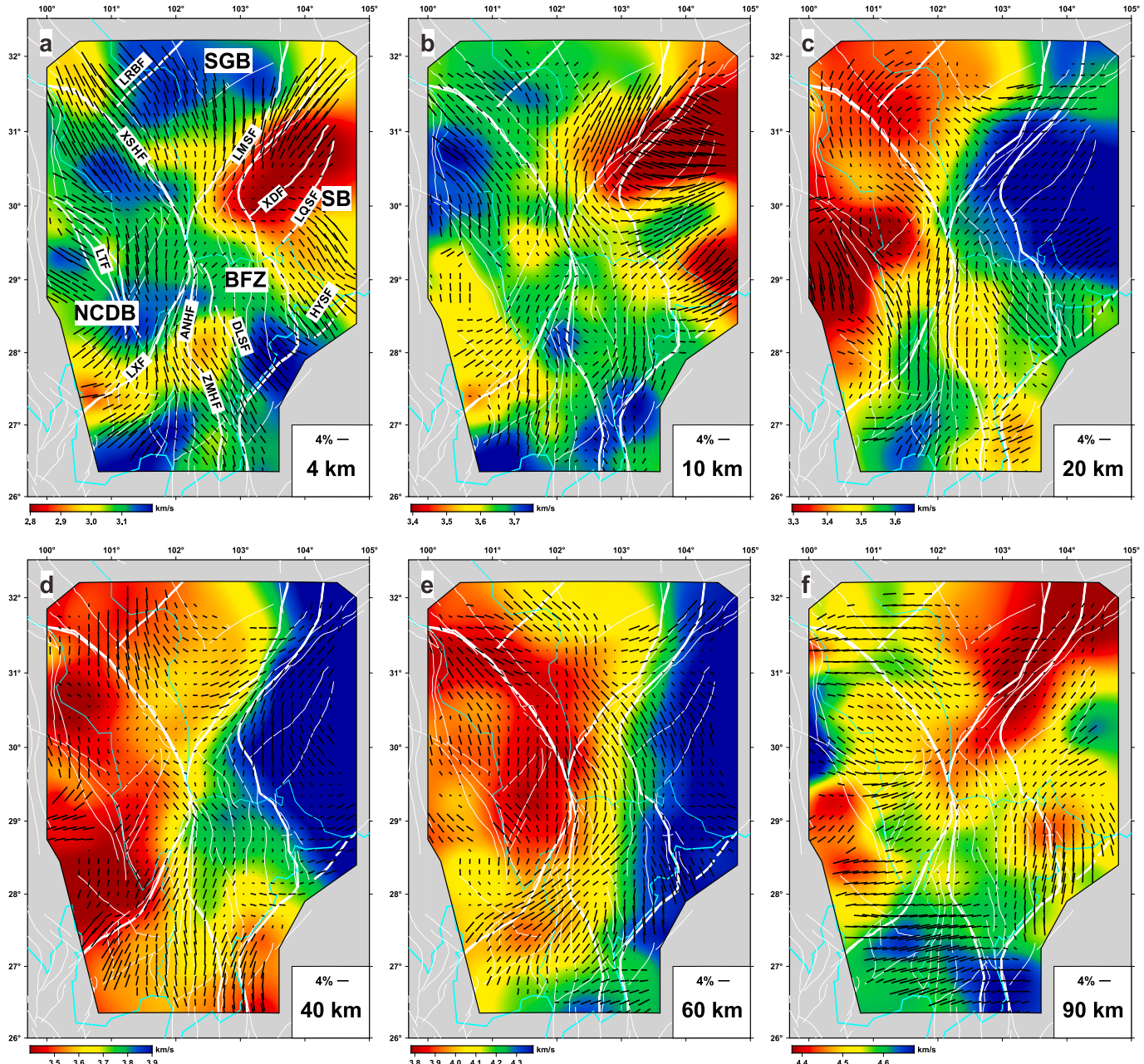


Fig. 11. Shear wave velocity (base maps) and azimuthal anisotropy (black bars) in different depth. The length and the direction of black bars represent the magnitude of anisotropy (MOA) and fast propagation density (FPD), respectively. ANHF: Anning He Fault; LMSF: Longmenshan Fault; XSHF: Xianshuuhe Fault; LXF: Lijiang-Xiaojin Fault; LTF: Litang fault; LRB: Longriba Fault; XDF: Xinjing-Deyang Fault; LQSF: Longquanshan Fault; HYSF: Huayingshan Fault; ZMHF: Zemuhe Fault; DLSF: Daliangshan Fault; BFZ: Block boundary fault zone; SGB: Songpan-Ganzi Block; SB: Sichuan Basin; NCDB: north Chuandian Block.

anisotropy of SKS splitting (Chang et al., 2015, 2017; Flesch et al., 2005; Huang et al., 2011, 2015; Lev et al., 2006; Liu et al., 2020; Ruan and Wang, 2002; Sol et al., 2007; Wang et al., 2008; Yang et al., 2018; Zhao et al., 2007, 2013). The blue rose diagrams in Fig. 13 show the angle differences of anisotropies between this study and the PmS phase; the medium values of the angle difference at depths of 2–20, 20–40, 40–60, and 2–60 km are approximately 25°, 31°, 31°, and 29°, respectively. The green rose diagrams in the same figure show the angle differences of anisotropies between this study and the SKS phase; the median values of the angle difference in the depth regions of 2–20, 20–40, 40–60, 60–100, and 2–100 km are approximately 26°, 31°, 26°, 31°, and 30°, respectively, suggesting that the crustal effect on SKS splitting cannot be neglected in the southeastern Tibetan Plateau.

In the layer of 2–20 km (Fig. 13a), weighted average anisotropies are

perpendicular to the horizontal direction of the maximum compressional stress in the collision zone along the LMSF and LXF (gray shaded area in Fig. 13a), but parallel to the fault strike and anticline/syncline axis (Fig. 13e), which suggests the SPO anisotropy. On the both side of the collision zone, the weighted average anisotropies of the SGB, NCDB and BFZ are consistent with the horizontal direction of the maximum compressive stress and the anisotropies of the PmS phases, suggesting the stress-induced anisotropy. In the 20–40 km layer (Fig. 13b), the consistent anisotropy between this study and the PmS phase appears in the SGB, SCDB, and NCDB; the consistent anisotropy between this study and SKS splitting appears in the SCDB, SGB, and the region between XSHF and LTF.

Interestingly, the anisotropies in the ELIP calculated using the Rayleigh wave (Liang et al., 2020; Cao F. et al., 2020; Zhang et al., 2021;

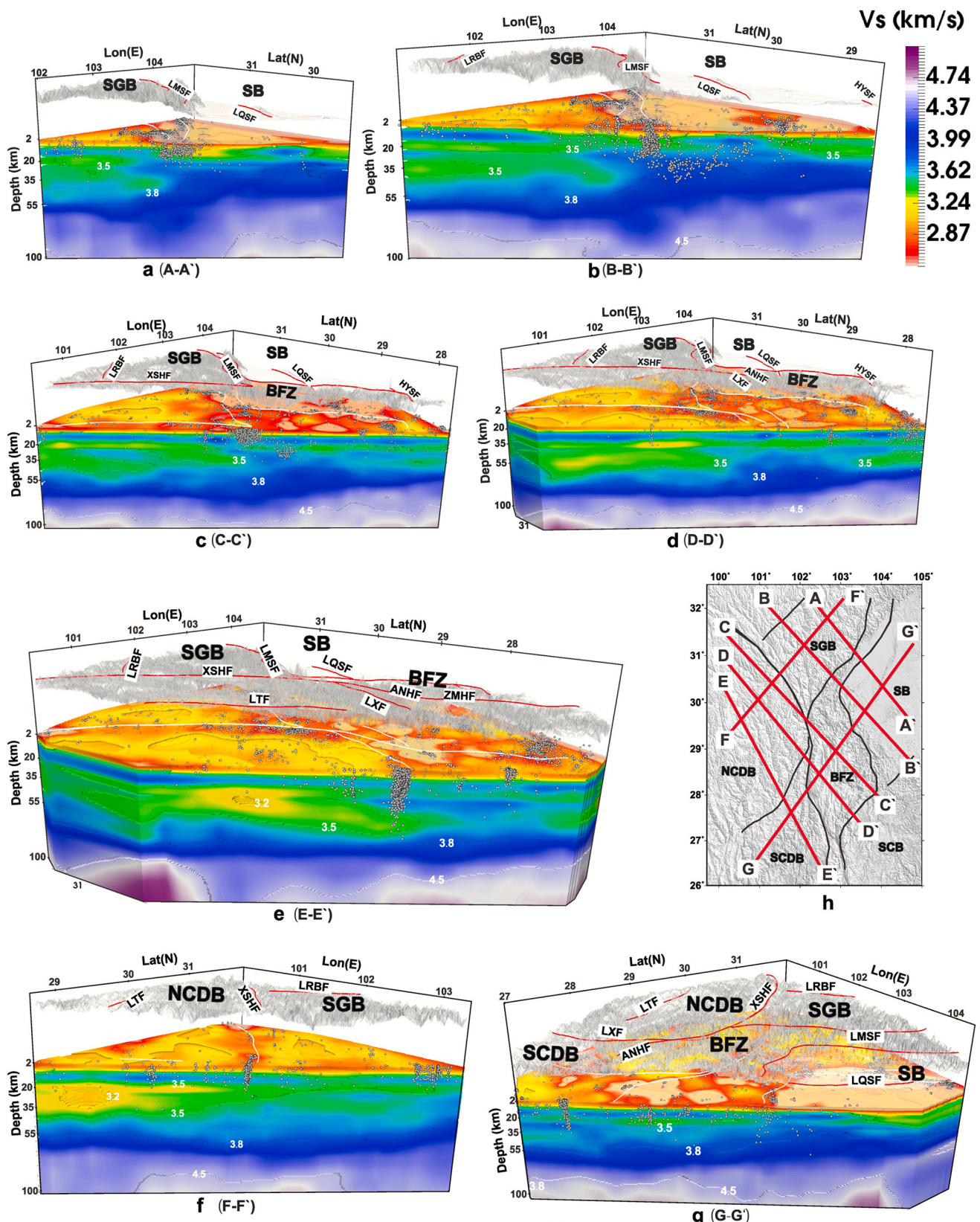


Fig. 12. Vertical profiles of Vs model. Profiles A–A' to G–G' are marked in subfigure h. The gray layers on the top of each profile denotes the topography. White lines and red lines are faults projected on the topography and on the Vs profiles, respectively. Gray dots mark the earthquakes with $M \geq 1.5$ (collected from China Seismic Experimental Site). SGB: Songpan-Ganzi Block; SB: Sichuan Basin; ANHF: Anning He Fault; LMSF: Longmenshan Fault; XSHF: Xianshuhe Fault; LXF: Lijiang-Xiaojin Fault; LTF: Litang fault; LRB: Longriba Fault; LQSF: Longquanshan Fault; HYSF: Huayingshan Fault; ZMHF: Zemuhe Fault; BFZ: Block boundary fault zone; SCDB: south Chuandian Block; NCDB: north Chuandian Block. (For interpretation of the references to colour in this figure legend, the reader is referred to the web version of this article.)

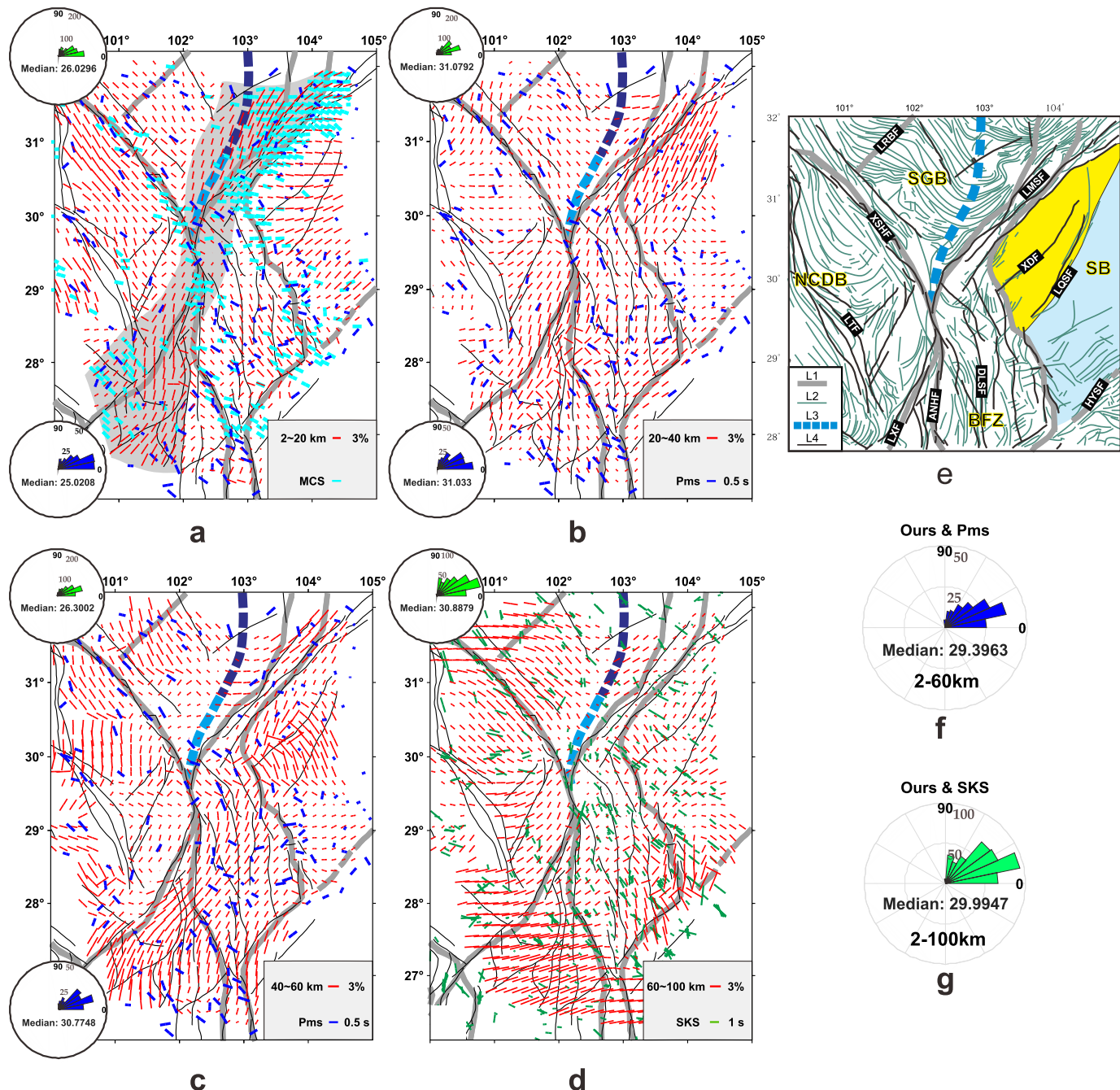


Fig. 13. Comparing the weighted average anisotropy of different depth ranges determined from this work with direction of the maximum compress stress, azimuthal anisotropies of PmS phase, SKS splitting, and the geological features. (a)–(d) The comparison for depth ranges of 2–20 km, 20–40 km, 40–60 km, and 60–100 km, respectively. Gray shadow in figure (a) marks the collision zone along the LMF and LXF. Thick gray lines are block boundaries; thin black lines represent faults; blue dashed line is the northwest edge of Yangtze crystalline basement determined by Guo et al. (2015); red bars are the weighted average anisotropy (this study); cyan bars are the maximum compress stress inverted by focal mechanism (Yang et al., 2018); blue bars represent the azimuthal anisotropies of PmS phase calculated by Zheng et al., 2018; green bars are the SKS splitting collected from <http://splitting.gm>. Blue rose diagrams represent the angular differences between the anisotropies of PmS phase and our results; green rose diagrams represent the angular differences between the anisotropies of SKS phase and our results. (e) Distribution of anticline/syncline axis (Burchfiel et al., 1995). (f) Angular differences between the anisotropies of PmS phase and ours in depth range of 2–60 km. (g) Angular differences between the anisotropies of SKS splitting and ours in depth range of 2–100 km. ANHF: Anning He Fault; LMSF: Longmenshan Fault; XSHF: Xianshuuhe Fault; LXF: Lijiang-Xiaojin Fault; LTF: Litang fault; LRBF: Longriba Fault; XDF: Xinjing-Deyang Fault; LQSF: Longquanshan Fault; HYSF: Huayingshan Fault; ZMHF: Zemuhe Fault; DLSF: Daliangshan Fault; BFZ: Block boundary fault zone; SGB: Songpan-Ganzi Block; SB: Sichuan Basin; NCDB: north Chuandian Block. (For interpretation of the references to colour in this figure legend, the reader is referred to the web version of this article.)

Wang et al., 2020) are different from those calculated using the PmS and SKS phases. The anisotropies obtained by PmS phase or SKS phase are more consistent with the maximum compressional stress direction (Fig. 13), and those obtained by Rayleigh wave phase are more consistent with orogen or fold axis in ELIP (Cao F. et al., 2020; Wang et al.,

2020). Despite the azimuthal anisotropy being jointly inverted by RFs and Rayleigh wave DCs in this study, the anisotropies of the mid-lower crust and upper mantle at the ELIP are still not consistent with those obtained individually by the PmS and SKS phases (Fig. 13). This difference suggests that the anisotropy in ELIP is extremely complicated; on

the other hand, the wavelength of the body wave is shorter than that of the surface wave, and seismic waves with different wavelengths are sensitive to different sizes of anisotropic structures (Faccenda et al., 2019; Wang et al., 2013a).

4.2. Deformation in the Sichuan Basin

The SB, located west of the Yangtze Block, has experienced multiple periods of tectonic evolution since the Sinian with a compressional folded crystal basement formed in the pre-Sinian (Li et al., 2014). From the Sinian to Triassic, Triassic to Jurassic, and Jurassic to the present, it has experienced regional extension (marine sediment), terrain uplift extension (terrestrial sediment), and compression, respectively (Li et al., 2019). Two subzones of the western Sichuan depression (yellow shadow in Fig. 13e) and southwestern Sichuan fold belt (light blue shadow in Fig. 13e) are present in our study area, where the former is bounded by LMSF and LQSF, and the latter is bounded by LQSF and HYSF, where there are massive folds with a fold strike of NE–SW (Fig. 13e; Burchfiel et al., 1995; Cheng et al., 2021).

The western Sichuan depression shows low Vs anomalies and small anisotropy magnitudes at a depth of 4 km (Fig. 11a), which is consistent with the nature of sediment that has not experienced intensive lateral deformation because the deformation between the southeast-extrusion SGB and the stable SB was absorbed by the high-dip-angle Longmenshan thrust fault in the shallow crust (Feng et al., 2016; Yang et al., 2018; Zhang et al., 2021). In the layer of 2–20 km depth, FPDs in the northern and western edges of the western Sichuan depression are consistent with the direction of maximum compressional stress determined from the focal mechanisms (Fig. 13a). This may imply that microfractures with strikes in the NWW–SEE directions in the upper crust are produced owing to the push from the Tibetan Plateau. Therefore, small earthquakes were recorded at the edge of the basin near the LMSF (gray dots in SB in Figs. 12a and 14).

For the southwestern Sichuan fold belt, FPDs at a depth of 4 km are

perpendicular to the anticline/syncline axis in the southwestern Sichuan fold belt (Fig. 11a; Fig. 13e; Burchfiel et al., 1995; Cheng et al., 2021), but are consistent with the direction of the maximum compressional stress. However, FPDs in the depth layer of 2–20 km (Fig. 13a) are consistent with the anticline/syncline axis and are sub-perpendicular to the direction of maximum compressional stress. This suggests that the stress-induced anisotropy appears in the shallow crust, and those in the upper crust may be the fossil anisotropy from the same tectonic event which resulted in the southwestern Sichuan fold belt.

In the mid-lower crust and upper mantle, SB shows as a strong and cold ancient craton with high velocity (Figs. 11, 12a, b; Liu et al., 2014; Liu et al., 2018; Liang et al., 2020), high density (Wang et al., 2007), low attenuation (Deng et al., 2021; He et al., 2021), and weak seismic activity (Liang et al., 2018). In addition, the MOA or FPD in mid-lower crust and upper mantle are bounded by LQSF or XDF, showing obvious partitioning properties (Fig. 13) and varying with depth, suggesting that the fossil anisotropy generated from different geological tectonic events. The inconsistent FPDs at different depths may correspond to the weak MOA of the PmS phase or SKS splitting in the SB. (Burchfiel et al., 1995; Cheng et al., 2021).

4.3. Deformation in the southeastern Tibetan Plateau

The SGB and NCDB are exposed to the same allochthon, which is composed mainly of a thick succession of strongly folded Mesozoic rocks characterized by upright to overturned folded and refolded flysch; the Jurassic granite is partially exposed inside the block (Wang, L. et al., 2013; Burchfiel et al., 1995). In the SCDB, BFZ, and LMSF, a large number of igneous rocks of different geological ages are exposed on the surface and intermingled with each other in bands, and the LMSF and LXF are the obvious gradient zones of the elevation and crustal thickness (Chen et al., 2021; Feng et al., 2020) and gravity anomalies (Liu et al., 2017). For example, from the SB across the LMSF to the SGB, the average elevation rose sharply from ~500 m to ~3500 m, and the crustal thickness changed from 40 km to 60 km (Feng et al., 2020). From the

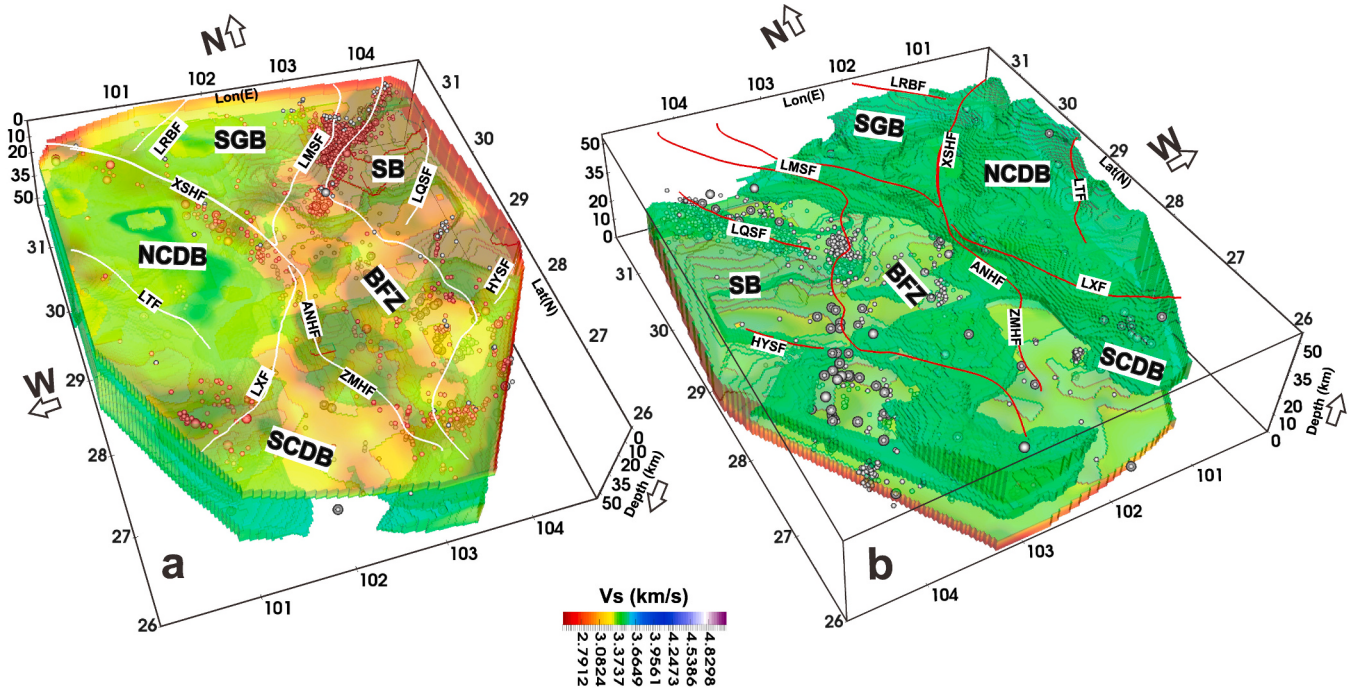


Fig. 14. The crustal low velocity zone in the southeastern Tibetan Plateau. Vs larger than 3.5 km/s are transparentized. (a) is looking downward from surface while (b) is a looking upward from depth. Small and relatively large silver balls are the earthquakes with magnitude $3 < M < 5$ and $M \geq 5$, respectively (China Seismic Experimental Site; Long et al., 2020). ANHF: Anning He Fault; LMSF: Longmenshan Fault; XSHF: Xianshuihe Fault; LXF: Lijiang-Xiaojin Fault; LTF: Litang fault; LRB: Longriba Fault; LQSF: Longquanshan Fault; HYSF: Huayingshan Fault; ZMHF: Zemuhe Fault; BFZ: Block boundary fault zone; SGB: Songpan-Ganzi Block; SB: Sichuan Basin; NCDB: north Chuandian Block; SCDB: south Chuandian Block.

SCDB across the LXF to the NCDB, the average elevation rises gradually from ~1000 m to ~3500 m, and the crustal thickness changes from 45 to 65 km.

As shown in Fig. 13a, the FPDs of the upper crust beneath the SGB and NCDB are parallel to the fault strike, anticline/syncline axis (Figs. 13e), and GNSS (Global Navigation Satellite System) velocity field (Figs. 1). Among them, faults and folds represent brittle shear deformation and continuous ductile deformation, respectively, implying that the deformation of the upper crust in the SGB and NCDB is controlled by both shearing deformation and continuous ductile deformation. The FPDs at different depths beneath the SGB, NCDB are consistent with each other (Fig. 13), and the anisotropy of the SKS and PmS phases in the northwest of the collision zone (Fig. 13a) are both consistent with the GNSS velocity direction (Fig. 1) and the direction of the maximum compressional stress of the upper crust (cyan bars in Fig. 13a), implying that deformations of the crust and upper mantle beneath the SGB and NCDB are generally coupled with each other. For smaller scales, FPDs in the northwest side of the LRBF, south segment of the LMSF, and LTF varied with depth, may indicating that local decoupling deformation exist in these areas.

As described in Section 3.2, our Vs model shows an obvious LVZ in the mid-lower crust of the SGB and NCDB (Fig. 11, 12), where there is high conductivity (Bai et al., 2010), attenuation (Deng et al., 2021; He et al., 2021), and Poisson ratio (Wang et al., 2015), implying that partial melts exist beneath the SGB and NCDB. However, the role of the LVZ in the mid-lower crust during plateau uplift remains controversial. The “pure shearing model” suggests that LVZ in the southeastern Tibetan Plateau plays a very weak role in the plateau uplift (Tappognier et al., 2001; Liang et al., 2020) while the “mid-lower crust flow model” suggests that the LVZ is driven by a lateral pressure gradient, flows east of central Tibet, accumulates and inflates at the flow front, buttressed by SB, and eventually leads to plateau uplift (Royden et al., 1997; Clark and Royden, 2000). In Fig. 14, Vs larger than 3.5 km/s in our model is made transparent. We observed that the LVZ beneath the collision zone along the LMSF and LXF (Fig. 13a) is thinner than that in the interior zone of SGB and NCDB; it gradually fades away along the LTF to LXF, and thins from SW-NE in the SGB (Fig. 12f, 14b), suggesting that the LVZ is not massively accumulated beneath the collision zones.

The comprehensive analyzes of multiple geological and geophysical data (Guo et al., 2013, 2014, and 2015) suggested that the Yangtze crystalline basement extends to the SGB beyond the northern segment of the LMSF to as far as the LRBF. It has been broken in a brittle manner and highly shortened from the early Triassic, and the strikes of the cracks are in the NE-SW direction (Guo et al., 2015). Our results show that the distribution of high Vs anomalies in the middle crust (Fig. 12a, b) and anisotropies in lithosphere (Fig. 13a–13d) are well constrained by the northwest edge of the Yangtze crystalline basement (marked by the blue dashed line in Fig. 13a–13e) and the inflection points of anticline/syncline axis of SGB (Fig. 13e). For example, from the SGB cross the northwest edge of the crystalline basement to LMSF, FPDs change from NW-SE to NE-SW in lithosphere (Fig. 13a–13c). We suggest that this anisotropy change may correspond to the existence of the crystalline basement beneath the SGB and the regulating effect of the crystalline basement on lithosphere deformation in Longmen Shan area.

In the region near the light blue dashed line in the SGB, FPDs in the upper crust (Fig. 13a) are consistent with fault strikes (Fig. 13e), but subperpendicular to the PDFs of the mid-lower crust, suggesting that the upper crust is decoupled from the mid-lower, and the consistent FPDs from the mid-lower crust to upper mantle imply a coupled deformation between the mid-lower crust and upper mantle in this area. The mid-lower crustal LVZ beneath the light blue dashed line is thicker than that beneath the deep blue dashed line (Fig. 12a); the southern segment of the LMSF is dominated by thrust faulting stress with plunges <30°, while the northern segment is mixed with focal mechanisms of normal, thrust, and strike-slip types (Yang et al., 2017, 2018). The different distribution of focal mechanisms between the southern and northern

segments of the LMSF may correspond to the difference in the distribution and deformation of the LVZ and crystalline basement. We suggest that the LVZ beneath the north side of the LMSF serves as a lubricant to detach the upper crust from the lower crust. This locally decouple deformation resulting in the thrust and fold belts in the upper crust of LMSF (Tappognier et al., 1982; Liang et al., 2020).

In the inner zone of the NCDB, the LVZ in the mid-lower crust was more prominent and thicker than that in the SGB (Fig. 12f, 14b). In the northeast of the LTF, anisotropies in the middle crust show a NE-SW FPDs (Fig. 13b), are subparallel to the FPDs of PmS phase, fast speed direction of SKS phase, strikes of minor faults and anticline/syncline axis (Fig. 13e), and are perpendicular to the directions of the GNSS velocity (Fig. 1) and the so-called flow direction along the LTF advocated by the “crust flow” model; anisotropies in lower crust and upper mantle show a nearly E-W FPDs. West of the LTF, anisotropies show a disorderly FPDs in the mid-lower crust and upper mantle. Collectively, the anisotropy in the mid-lower crust beneath the inner zone of the NCDB contradicts the crust flow model.

Paleo-elevation studies suggest that central Tibet was formed as a proto-plateau (elevation >3000 m) in the Late Cretaceous (Hu et al., 2020) and Qiangtang reached ~5000 m by at least the middle Oligocene (Xu et al., 2013). A high proto elevation in central Tibet in the Late Cretaceous suggests a sufficient lateral pressure gradient in the southeastern Tibetan Plateau. The plateau uplift has very weak crustal shortening and a low topographic gradient from the NCDB to the SCDB (Royden et al., 1997). Coupled with the existence of partial melts and high heat flow in the NCDB and SGB, this seems to meet the “crust flow” model.

However, the study of the relationship between crustal thicknesses, Vp/Vs ratios, and silica content indicates that a high-viscosity LVZ exists in the mid-lower crust beneath central Tibet (Liu et al., 2021); the crustal LVZ is frequently related to the high topography and the distribution of LVZ in the upper mantle (Liang et al., 2004, 2020); and Bao et al. (2020) observed that the anisotropies of the mid-lower crust are disordered and weaker beneath the plateau. The above evidence contradicts the crustal flow model. We then suggest that the LVZ of the mid-lower crust beneath the southeastern Tibetan Plateau could have been generated locally. P-wave tomography (Huang et al., 2019; Feng et al., 2022; Wang et al., 2021) and the thermo-rheological structure (Chen et al., 2014) suggest that lithospheric delamination exists beneath the southeastern Tibetan Plateau. Under the dual disturbance of the lithospheric dismantling and the subduction of the Indian plate to the asthenosphere materials, the rising hot materials of the asthenosphere heated and weaken the crust (Wang et al., 2021; Hou et al., 2021), and then resulted in a prominent LVZ and disordered FPDs in the mid-lower crust beneath the inner zone of the NCDB (Fig. 13b and c). This deformation mechanism is consistent with the geochemical studies—according to the high $^{87}\text{Sr}/^{86}\text{Sr}$ ratio and low ϵNd (neodymium isotopic composition) value, the magma source of the Tibetan Plateau and its margin regions are mainly from the partial melting of an metasomatic enriched lithospheric mantle with asthenosphere components and the partial melting of an refertilized juvenile lower crust (or crust mantle transitional zone) during the late period of Indian-Eurasian collision (40–26 Ma) (Jiang et al., 2006; Hou et al., 2017; Zhang, 2018; Hou et al. 2020).

The ELIP is located in the southern margin of the SB and is widely exposed to Late Permian flood basalt (Fig. 1). Volcanism began at approximately 260 Ma (Huang et al., 2022). SCDB and BFZ are located in the inner and intermediate zones, respectively (Fig. 1). In the upper crust, the wide distribution of high Vs anomalies in the SCDB and NCDB is associated with the widely exposed Late Permian Emeishan flood basalts. The FPDs in the upper crust beneath the SCDB are consistent with the fault strike and anticline/syncline axis, however, those beneath the BFZ are more consistent with the direction of the maximum compressional stress (Fig. 13a). This difference indicates that the BFZ exists masses of stress-induced microcracks in the upper crust, and have

experienced more severe brittle deformation than the interior zone of SCDB. The BFZ is pushed by the NCDB and SGB and blocked by the Yangtze Craton, resulting in internal rupture and massive stress-parallel microcracks. However, the deformation of SCDB is largely absorbed by the LXF in the north and the ANHF and ZMHF in the east (Xu et al., 2003). Weaker seismic activity inside the SCDB (Fig. 13) and a lower GNSS velocity inside the BFZ (Fig. 1a) can explain the difference in deformation between the SCDB and the BFZ.

A mushroom-shaped high-velocity structure with a northeast-trending distribution in the mid-lower crust and upper mantle beneath the SCDB and BFZ (Fig. 12c–12e, 12 g, and 14) indicates the magmatic pool of the Emeishan paleo-mantle plume, and is consistent with the paleo-mantle plume with high P-wave and S-wave velocity (Xu et al., 2015; Zhang et al., 2020; Liu et al., 2021), high resistivity (Li et al., 2020), low attenuation (He et al., 2021; Deng et al., 2020), and high Bouguer gravity anomalies (Shi et al., 2015; Xu et al., 2015) beneath the SCDB. The mantle plumes rising from the deeper Earth have higher densities than the surrounding rocks and display high-strength and high-density rigid blocks after cooling. Its existence blocks the southward movement of the NCDB and prevents the LVZ beneath the NCDB from extending to the south (Zhang et al., 2020; Li et al., 2020), which may help to generate the LXF. The consistent FPD in the crust of the LXF may indicate that the LXF is a deep fault cutting through the crust (Fig. 13).

5. Conclusions

In this study, a series of auto-seismic data processing methods were applied to ANT and WGM. We take advantage of the different sensitivities of WGM and ANT to extend the period length of the dispersion curve. An azimuth-dependent joint inversion method was proposed for joint inversion of the surface dispersion curve and receiver function. Applying this method to the TWSA, we obtained a high-resolution 3D Vs model and azimuthal anisotropic structure of the southeastern Tibetan Plateau.

Anisotropies in the SB are divided into different type according to the MOAs or FPDs by the XDF and LMSF, suggesting that the fossil anisotropy were generated from different geological tectonic events.

The LVZ in the interior zone of the SGB and NCDB was thicker than that in the colliding zones along the LMSF and LXF, indicating that the LVZ was not massively accumulated during plateau uplift. The anisotropies with disordered FPDs in the mid-lower crust and upper mantle against the crust flow model, suggest that the mid-lower crustal LVZ in the southeastern Tibetan Plateau is generated locally.

The distribution of velocity and anisotropy in the vicinity of LMSF suggest that the crystalline basement of Yangtze block may have under-thrust northwestward to lay below SGB. This is consistent with the proposed Yangtze basement edge by Guo et al. (2013, 2104 and 2015).

The mushroom-shaped high-velocity structure beneath the SCDB and BFZ may be the relic of the cold Emeishan paleo-mantle plume and acts as a barrier for the southeastward movement of the NCDB.

Open research

We accessed seismic waveforms using CSADMC <http://www.chinarraydmc.cn/> (doi:10.12001/ChinArray.Data).

The programs for Auto WG analysis and the ADJI method can be accessed from <https://doi.org/10.5281/zenodo.6516480>. The dataset of azimuth-dependent dispersion curves can be accessed from <https://doi.org/10.5281/zenodo.6519337>. A 3D Vs model and azimuthal anisotropic structure of the southeastern Tibetan Plateau are provided as supporting materials.

CRediT authorship contribution statement

Feihuang Cao: Conceptualization, Methodology, Software,

Validation, Formal analysis, Investigation, Data curation, Writing – original draft, Visualization, Project administration. **Chuntao Liang:** Conceptualization, Methodology, Software, Validation, Supervision, Funding acquisition, Writing – review & editing. **Yihai Yang:** Software. **Lu Zhou:** Software. **Zhiqiang Liu:** Visualization. **Zhen Liu:** Writing – review & editing.

Declaration of Competing Interest

The authors declare that they have no known competing financial interests or personal relationships that could have appeared to influence the work reported in this paper.

Data availability

The authors do not have permission to share data.

Acknowledgments

We appreciate Professor Chen Lin and the three anonymous reviewers for their constructive comments and suggestions, which have helped improve this paper. Seismic waveforms were provided by the China Seismic Array Data Management Center (CSADMC) of the Institute of Geophysics, China Earthquake Administration. Parts of Ambient Noise Analysis programs was accessed from Yao Lab (<http://yaolab.ustc.edu.cn/resources.php?i=28>). The earthquake catalog was accessed from the China Seismic Experimental Site (<http://cses.ac.cn/sjcp/gmx/2021/132.shtml>). This study was partially supported by the Chinese National Science Foundation (Grant Nos. 42174071 and 42074068) and the National Key Research and Development Program of China (Grant No. 2018YFC1503401).

Appendix A. Supplementary data

Supplementary data to this article can be found online at <https://doi.org/10.1016/j.tecto.2022.229690>.

References

- Backus, G.E., 1965. Possible forms of seismic anisotropy of the uppermost mantle under oceans. *J. Geophys. Res.* 70 (14), 3429–3439. <https://doi.org/10.1029/jz070i014p03429>.
- Bai, D., Unsworth, M.J., Meju, M.A., Ma, X., Teng, J., Kong, X., Sun, Y., Sun, J., Wang, L., Jiang, C., Zhao, C., Xiao, P., Liu, M., 2010. Crustal deformation of the eastern Tibetan plateau revealed by magnetotelluric imaging. *Nat. Geosci.* 3 (5), 358–362. <https://doi.org/10.1038/ngeo830>.
- Bao, X., Song, X., Eaton, D.W., Xu, Y., Chen, H., 2020. Episodic Lithospheric Deformation in Eastern Tibet Inferred from Seismic Anisotropy. *Geophys. Res. Lett.* 47 (3) <https://doi.org/10.1029/2019GL085721>.
- Bodin, T., Sambridge, M., Tkalcic, H., Arroucau, P., Gallagher, K., Rawlinson, N., 2012. Transdimensional inversion of receiver functions and surface wave dispersion. *Journal of Geophysical Research: Solid Earth* 117 (2), 1–24. <https://doi.org/10.1029/2011JB008560>.
- Bodin, T., Leiva, J., Romanowicz, B., Maupin, V., Yuan, H., 2016. Imaging anisotropic layering with Bayesian inversion of multiple data types. *Geophys. J. Int.* 206 (1), 605–629. <https://doi.org/10.1093/gji/GJW124>.
- Burchfiel, B.C., Zhiliang, C., Yuping, L., Royden, L.H., 1995. Tectonics of the Longmen Shan and Adjacent Regions, Central China. *International Geology Review* 37 (8), 661–735. <https://doi.org/10.1080/00206819509465424>.
- Campillo, M., Paul, A., 2003. Long-Range Correlations in the Diffuse Seismic Coda. *Science* 299 (5606), 547–549. Available at: <http://www.jstor.org/stable/3833286>.
- Cao, F., Liang, C., Zhou, L., Zhu, J., 2020b. Seismic Azimuthal Anisotropy for the Southeastern Tibetan Plateau Extracted by Wave Gradiometry Analysis. *Journal of Geophysical Research: Solid Earth* 125 (5). <https://doi.org/10.1029/2019JB018395>.
- Cao, R., Earp, S., De Ridder, S.A.L., Curtis, A., Galetti, E., 2020a. Near-real-time near-surface 3D seismic velocity and uncertainty models by wavefield gradiometry and neural network inversion of ambient seismic noise. *Geophysics* 85 (1), KS13–KS27. <https://doi.org/10.1190/geo2018-0562.1>.
- Chang, L., Flesch, L.M., Wang, C.Y., Ding, Z., 2015. Vertical coherence of deformation in lithosphere in the eastern Himalayan syntaxis using GPS, Quaternary fault slip rates, and shear wave splitting data. *Geophys. Res. Lett.* 42 (14), 5813–5819. <https://doi.org/10.1002/2015GL064568>.
- Chang, L., Ding, Z., Wang, C., Flesch, L.M., 2017. Vertical coherence of deformation in lithosphere in the NE margin of the Tibetan plateau using GPS and shear-wave

- splitting data. *Tectonophysics* 699, 93–101. <https://doi.org/10.1016/j.tecto.2017.01.025>.
- Chang, Y., Liang, C., Cao, F., Zhou, L., Liao, J., Lu, W., Wang, C., 2022. Seismic Velocity Structure for the Anninghe - Zemuhe Fault Zone by Wave Gradiometry Analysis. *Chin. J. Geophys.* <https://doi.org/10.6038/cjg2022P0731>.
- Chen, L., Berntsson, F., Zhang, Z., Wang, P., Wu, J., Xu, T., 2014. Seismically constrained thermo-rheological structure of the eastern Tibetan margin: Implication for lithospheric delamination. *Tectonophysics* 627, 122–134. <https://doi.org/10.1016/j.tecto.2013.11.005>.
- Chen, L.Y., Wang, W., Zhang, L., 2021. Crustal thickness in Southeast Tibet based on the swchinacvm-1.0 model. *Earthquake Science* 34 (3), 246–260. <https://doi.org/10.29382/eqs-2021-0010>.
- Cheng, G., Jiang, B., Li, M., Li, F., Zhu, M., 2021. Structural evolution of southern Sichuan Basin (South China) and its control effects on tectonic fracture distribution in Longmaxi shale. *J. Struct. Geol.* 153, 104465 <https://doi.org/10.1016/j.jsg.2021.104465>.
- ChinArray, 2006. China Seismic Array waveform data. China Earthquake Administration. <https://doi.org/10.12001/ChinArray.Data>.
- Chong, J., Ni, S., Zhao, L., 2015. Joint Inversion of Crustal Structure with the Rayleigh Wave phase Velocity Dispersion and the ZH Ratio. *Pure Appl. Geophys.* 172 (10), 2585–2600. <https://doi.org/10.1007/s0024-014-0902-z>.
- Clark, M.K., Royden, L.H., 2000. Topographic ooze: building the eastern margin of Tibet by lower crustal flow. *Geology* 28 (8), 703–706. [https://doi.org/10.1130/0091-7613\(2000\)28<703:TOBTEM>2.0.CO;2](https://doi.org/10.1130/0091-7613(2000)28<703:TOBTEM>2.0.CO;2).
- Clark, M.K., Schoenbohm, L.M., Royden, L.H., Whipple, K.X., Burchfiel, B.C., Zhang, X., Tang, W., Wang, E., Chen, L., 2004. Surface uplift, tectonics, and erosion of eastern Tibet from large-scale drainage patterns. *Tectonics* 23 (1), 1–21. <https://doi.org/10.1029/2002TC001402>.
- Crampin, S., 1981. A review of wave motion in anisotropic and cracked elastic-media. *Wave Motion* 3 (4), 343–391. [https://doi.org/10.1016/0165-2125\(81\)90026-3](https://doi.org/10.1016/0165-2125(81)90026-3).
- Crampin, S., 1984. An introduction to wave propagation in anisotropic media. *Geophys. J. R. Astron. Soc.* 76 (1), 17–28. <https://doi.org/10.1111/j.1365-246X.1984.tb05018.x>.
- Cupillard, P., Stehly, L., Romanowicz, B., 2011. The one-bit noise correlation: a theory based on the concepts of coherent and incoherent noise. *Geophys. J. Int.* 184 (3), 1397–1414. <https://doi.org/10.1111/j.1365-246X.2010.04923.x>.
- De Ridder, S.A.L., Curtis, A., 2017. Seismic gradiometry using ambient seismic noise in an anisotropic Earth. *Geophys. J. Int.* 209 (2), 1168–1179. <https://doi.org/10.1093/gji/gjx073>.
- Deng, B., Liu, S., Jiang, L., Zhao, G., Huang, R., Li, Z., Li, J., Jansa, L., 2018. Tectonic uplift of the Xichang Basin (SE Tibetan Plateau) revealed by structural geology and thermochronology data. *Basin Res.* 30 (1), 75–96. <https://doi.org/10.1111/bre.12243>.
- Deng, Q., Zhang, P., Ran, Y., Yang, X., Min, W., Chen, L., 2003. Active tectonics and earthquake activities in China. *Earth Science Frontiers* 10 (S1), 66–73. https://en.cnki.com.cn/Article_en/CJFDTotal-DXQY2003S1011.htm.
- Deng, Y., Byrnes, J.S., Bezada, M., 2021. New Insights into the Heterogeneity of the Lithosphere-Asthenosphere System beneath South China from Teleseismic Body-Wave Attenuation. *Geophys. Res. Lett.* 48 (6) <https://doi.org/10.1029/2020GL091654> e2020GL091654.
- Efron, B., 1979. Bootstrap Methods: another look at the Jackknife. *Ann. Statist* 7 (1), 1–26. January. <https://doi.org/10.1214/aos/1176344552>.
- Faccenda, M., Ferreira, A.M.G., Tisato, N., Lithgow-Bertelli, C., Stixrude, L., Pennacchioni, G., 2019. Extrinsic Elastic Anisotropy in a Compositionally Heterogeneous Earth's Mantle. *Journal of Geophysical Research: Solid Earth* 124 (2), 1671–1687. <https://doi.org/10.1029/2018JB016482>.
- Feng, J., Yao, H., Chen, L., Wang, W., 2022 April. Massive lithospheric delamination in southeastern Tibet facilitating continental extrusion. *National Science Review* 9 (4). <https://doi.org/10.1093/nsr/nwab174> nwab174.
- Feng, M., An, M., Mechie, J., Zhao, W., Xue, G., Su, H., 2020. Lithospheric structures of and tectonic implications for the central-east Tibetan plateau inferred from joint tomography of receiver functions and surface waves. *Geophys. J. Int.* 223 (3), 1688–1707. <https://doi.org/10.1093/gji/gja403>.
- Feng, S., Zhang, P., Liu, B., Wang, M., Zhu, S., Ran, Y.K., Wang, W., Zhang, Z., Zheng, W., Zheng, D., Zhang, H., Tian, X., 2016. Deep crustal deformation of the Longmen Shan, eastern margin of the Tibetan Plateau, from seismic reflection and Finite Element modeling. *Journal of Geophysical Research: Solid Earth* 121 (2), 767–787. <https://doi.org/10.1002/2015JB012352>.
- Flesch, L.M., Holt, W.E., Silver, P.G., Stephenson, M., Wang, C.Y., Chan, W.W., 2005. Constraining the extent of crust-mantle coupling in Central Asia using GPS, geologic, and shear wave splitting data. *Earth Planet. Sci. Lett.* 238 (1–2), 248–268. <https://doi.org/10.1016/j.epsl.2005.06.023>.
- Forsyth, D.W., Webb, S.C., Dorman, L.M., Shen, Y., 1998. Phase Velocities of Rayleigh Waves in the MELT Experiment on the East Pacific rise. *Advancement of Science* 280 (5367), 1235–1238. <https://doi.org/10.1126/science.280.5367.1235>.
- Gan, W., Zhang, P., Shen, Z.K., Niu, Z., Wang, M., Wan, Y., Zhou, D., Cheng, J., 2007. Present-day crustal motion within the Tibetan Plateau inferred from GPS measurements. *Journal of Geophysical Research: Solid Earth* 112 (8), 1–14. <https://doi.org/10.1029/2005JB004120>.
- Gao, Y., Shi, Y., Chen, A., 2018. Crustal seismic anisotropy and compressive stress in the eastern margin of the Tibetan Plateau and the influence of the MS8.0 Wenchuan earthquake. *Kexue Tongbao/Chinese. Science Bulletin* 63 (19), 1934–1948. <https://doi.org/10.1360/N972018-00317>.
- Geological Bureau of Sichuan Province, 2014. Geological Map of Sichuan at 1/2750,000: Beijing. Geol. Publ. House.
- Guo, B., et al., 2009. Teleseismic P-wave tomography of the crust and upper mantle in Longmenshan area, West Sichuan. *Chinese Journal of Geophysics* (in Chinese) 52 (2), 346–355. Available at: http://www.geophy.cn/article/id/cjg_914.
- Guo, X., Gao, R., Randy Keller, G., Xu, X., Wang, H., Li, W., 2013. Imaging the crustal structure beneath the eastern Tibetan Plateau and implications for the uplift of the Longmen Shan range. *Earth Planet. Sci. Lett.* 379, 72–80. <https://doi.org/10.1016/j.epsl.2013.08.005>.
- Guo, X., Keller, G.R., Gao, R., Xu, X., Wang, H., Li, W., 2014. Irregular western margin of the Yangtze block as a cause of variation in tectonic activity along the Longmen Shan fault zone, eastern Tibet. *Int. Geol. Rev.* 56 (4), 473–480. <https://doi.org/10.1080/00206814.2013.873358>.
- Guo, X., Gao, R., Xu, X., Keller, G.R., Yin, A., Xiong, X., 2015. Longriba fault zone in eastern Tibet: An important tectonic boundary marking the westernmost edge of the Yangtze block. *Tectonics* 34 (5), 970–985. <https://doi.org/10.1002/2015TC003880>.
- He, F., Liang, C., Yang, Y., Fang, L., Su, J., 2017. The crust structure of the unruptured segment between Wenchuan and Lushan earthquake revealed by Receiver Functions. *Chin. J. Geophys.* 60 (6), 2130–2146. <https://doi.org/10.6038/cjg20170609>.
- He, X., Zhao, L.F., Xie, X.B., Tian, X., Yao, Z.X., 2021. Weak Crust in Southeast Tibetan Plateau Revealed by Lg-Wave Attenuation Tomography: Implications for Crustal Material Escape. *Journal of Geophysical Research: Solid Earth* 126 (3), 1–17. <https://doi.org/10.1029/2020JB020748>.
- Herrmann, R.B., Ammon, C., 2004. Surface waves, receiver functions and crustal structure, Computer programs in Seismology. *Structure*, June 133, 135. http://www.eas.slu.edu/eqc/eqc_cps/CPS330/cps330c.pdf.
- Herrmann, R.B., Ammon, C.J., 2002. Computer Programs in Seismology—Surface Waves, St Louis Univ., Receiver Functions and Crustal Structure. St. Louis, Mo.
- Hou, Z., Zhou, Y., Wang, R., 2017. Recycling of metal-fertilized lower continental crust: Origin of non-arc Au-rich porphyry deposits at cratonic edges. *Geology* 45, 563–566. <https://doi.org/10.1130/G38619.1>.
- Hou, Z., Xu, B., Zheng, Y., et al., 2021. Mantle flow: the deep mechanism of large-scale growth in Tibetan Plateau (in Chinese). *Chin. Sci. Bull.* 66, 2671–2690. <https://doi.org/10.1360/TB-2020-0817>.
- Hu, F., Wu, F., Chapman, J.B., Dueca, M.N., Ji, W., Liu, S., 2020. Quantitatively Tracking the Elevation of the Tibetan Plateau since the cretaceous: Insights from Whole-Rock Sr/Y and La/Y Ratios. *Geophys. Res. Lett.* 47 (15), 1–10. <https://doi.org/10.1029/2020GL089202>.
- Huang, Z., Wang, L., Xu, M., Ding, Z., Wu, Y., Wang, P., Mi, N., Yu, D., Li, H., 2015. Teleseismic shear-wave splitting in SE Tibet: Insight into complex crust and upper-mantle deformation. *Earth Planet. Sci. Lett.* 432, 354–362. <https://doi.org/10.1016/j.epsl.2015.10.027>.
- Huang, Z., Wang, L., Xu, M., Zhao, D., Mi, N., Yu, D., 2019. P and S Wave Tomography Beneath the SE Tibetan Plateau: evidence for Lithospheric Delamination. *J. Geophys. Res. Solid Earth* 124 (10), 10292–10308. <https://doi.org/10.1029/2019JB017430>.
- Huang, Z.C., Wang, L., Zhao, D., Mi, N., Xu, M., 2011. Seismic anisotropy and mantle dynamics beneath China. *Earth Planet. Sci. Lett.* 306 (1–2), 105–117. <https://doi.org/10.1016/J.EPSL.2011.03.038>.
- Jiang, Y., Jiang, S., Ling, H., 2006. Low-degree melting of a metasomatized lithospheric mantle for the origin of Cenozoic Yulong monzogranite-porphyry, East Tibet: Geochemical and Sr-Nd-Pb-Hf isotopic constraints. *Earth Planet. Sci. Lett.* 241, 617–633. <https://doi.org/10.1016/j.epsl.2005.11.023>.
- Julia, J., Ammon, C.J., Herrmann, R.B., Correig, A.M., 2000. Joint inversion of receiver function and surface wave dispersion observations. *Geophys. J. Int.* 143 (1), 99–112. <https://doi.org/10.1046/j.1365-246X.2000.00217.x>.
- Klemperer, S.L., 2006. Crustal flow in Tibet: Geophysical evidence for the physical state of Tibetan lithosphere, and inferred patterns of active flow. *Geol. Soc. Spec. Publ.* 268 (2), 39–70. <https://doi.org/10.1144/GSL.SP.2006.268.01.03>.
- Kong, F., Wu, J., Liu, K.H., Gao, S.S., 2016. Crustal anisotropy and ductile flow beneath the eastern Tibetan Plateau and adjacent areas. *Earth Planet. Sci. Lett.* 442, 72–79. <https://doi.org/10.1016/J.EPSL.2016.03.003>.
- Langston, C.A., 1977. The effect of planar dipping structure on source and receiver responses for constant ray parameter. *Bull. Seismol. Soc. Am.* 67 (4), 1029–1050. <https://doi.org/10.1785/BSSA0670041029>.
- Langston, C.A., 2007a. Spatial gradient analysis for linear seismic arrays. *Bull. Seismol. Soc. Am.* 97 (1 B), 265–280. <https://doi.org/10.1785/0120060100>.
- Langston, C.A., 2007b. Wave gradiometry in the time domain. *Bull. Seismol. Soc. Am.* 97 (3), 926–933. <https://doi.org/10.1785/0120060152>.
- Langston, C.A., 2007c. Wave gradiometry in two dimensions. *Bull. Seismol. Soc. Am.* 97 (2), 401–416. <https://doi.org/10.1785/0120060138>.
- Langston, C.A., Ayele, M.M., 2016. Vertical seismic wave gradiometry: Application at the San Andreas fault Observatory at depth. *Geophysics* 81 (3), D233–D243. <https://doi.org/10.1190/GEO2015-0404.1>.
- Lev, E., Long, M.D., van der Hilst, R.D., 2006. Seismic anisotropy in Eastern Tibet from shear wave splitting reveals changes in lithospheric deformation. *Earth Planet. Sci. Lett.* 251 (3–4), 293–304. <https://doi.org/10.1016/j.epsl.2006.09.018>.
- Li, C., van der Hilst, R.D., Meltzer, A.S., Engdahl, E.R., 2008. Subduction of the Indian lithosphere beneath the Tibetan Plateau and Burma. *Earth Planet. Sci. Lett.* 274 (1–2), 157–168. <https://doi.org/10.1016/j.epsl.2008.07.016>.
- Li, C.X., He, D., Sun, Y., He, J., Jiang, Z., 2014a. Structural characteristic and origin of intra-continental fold belt in the eastern Sichuan basin, South China Block. *J. Asian Earth Sci.* 111, 206–221. <https://doi.org/10.1016/J.JSEAES.2015.07.027>.
- Li, H.K., Li, Z., Long, W., Wan, S., Ding, X., Wang, S., Wang, Q., 2019. Vertical configuration of Sichuan Basin and its superimposed characteristics of the prototype basin. *Journal of Chengdu University of Technology (Science and Technology Edition)* 46 (3), 257–267. <https://doi.org/10.3969/j.issn.1671-9727.2019.03.01>.

- Li, H.Y., Su, W., Wang, C.Y., Huang, Z., Lv, Z., 2010a. Ambient noise love wave tomography in the eastern margin of the Tibetan plateau. *Tectonophysics* 491 (1–4), 194–204. <https://doi.org/10.1016/j.tecto.2009.12.018>.
- Li, X., Ma, X., Chen, Y., Xue, S., Varentsov, I.M., Bai, D., 2020. A plume-modified lithospheric barrier to the southeastward flow of partially molten Tibetan crust inferred from magnetotelluric data. *Earth Planet. Sci. Lett.* 548, 116493 <https://doi.org/10.1016/j.epsl.2020.116493>.
- Li, Y., Yao, H.J., Liu, Q.Y., Chen, J.H., 2010b. Phase velocity array tomography of Rayleigh waves in western Sichuan from ambient seismic noise. *Chinese Journal of Geophysics (in Chinese)* 53 (4), 842–852. <https://doi.org/10.3969/j.issn.001-5733.2010.04.009>.
- Li, Z., Ma, C., Ying, D., Li, H., Li, Y., Wang, S., Xi, Y., 2014b. Tectonic dynamic evolution and analysis of basin-range coupling and basin-mountain coupling in Sichuan-Chongqing region, China. *Acta Petralogica Sinaca* 30 (03), 631–640. <http://www.yxb.ac.cn/article/id/aps.20140303>.
- Liang, C.T., Langston, C.A., 2009a. Wave gradiometry for USArray: Rayleigh waves. *Journal of Geophysical Research: Solid Earth* 114 (2), 1–19. <https://doi.org/10.1029/2008jb005918>.
- Liang, C.T., Langston, C.A., 2009b. Three-dimensional crustal structure of eastern North America extracted from ambient noise. *J. Geophys. Res.* 114, B03310. <https://doi.org/10.1029/2008JB005919>.
- Liang, C.T., Song, X., Huang, J., 2004. Tomographic inversion of Pn travel times in China. *Journal of Geophysical Research: Solid Earth* 109 (11), 1–19. <https://doi.org/10.1029/2003JB002789>.
- Liang, C.T., Huang, Y., Wang, C., Liu, Z., Yang, Y., Wu, J., He, F., 2018. Progress in the studies of the seismic gap between the 2008 Wenchuan and 2013 Lushan earthquakes. In: *Chin. J. Geophys.* 61 (5), 1996–2010. <https://doi.org/10.6038/cjg2018M0254>.
- Liang, C.T., Liu, Z., Hua, Q., Wang, L., Jiang, N., Wu, J., 2020. The 3D Seismic Azimuthal Anisotropies and Velocities in the Eastern Tibetan Plateau Extracted by an Azimuth-Dependent Dispersion Curve Inversion Method. *Tectonics* 39 (4). <https://doi.org/10.1029/2019TC005747>.
- Ligorría, J.P., Ammon, C.J., 1999. Iterative deconvolution and receiver-function estimation. *Bull. Seismol. Soc. Am.* 89 (5), 1395–1400. <https://doi.org/10.1785/bssa0890051395>.
- Lin, F.C., Ritzwoller, M.H., 2011. Helmholtz surface wave tomography for isotropic and azimuthally anisotropic structure. *Geophys. J. Int.* 186 (3), 1104–1120. <https://doi.org/10.1111/j.1365-246X.2011.05070.x>.
- Lin, F.C., Ritzwoller, M.H., Snieder, R., 2009. Eikonal tomography: Surface wave tomography by phase front tracking across a regional broad-band seismic array. *Geophys. J. Int.* 177 (3), 1091–1110. <https://doi.org/10.1111/j.1365-246X.2009.04105.x>.
- Liu, B., Zhou, Y., Yang, G., 2017. Characteristics of isostatic gravity anomaly in Sichuan-Yunnan region, China. *Geodesy and Geodynamics* 8 (4), 238–245. <https://doi.org/10.1016/j.geog.2017.04.002>.
- Liu, H., Niu, F., 2012. Estimating crustal seismic anisotropy with a joint analysis of radial and transverse receiver function data. *Geophys. J. Int.* 188 (1), 144–164. <https://doi.org/10.1111/j.1365-246X.2011.05249.x>.
- Liu, J., Wu, J., Wang, W., Fang, L., Chang, K., 2020. Seismic anisotropy beneath the eastern margin of the Tibetan Plateau from SKS splitting observations. *Tectonophysics* 785 (October 2019), 228430. <https://doi.org/10.1016/j.tecto.2020.228430>.
- Liu, Q.Y., Li, Y., Chen, J.H., Guo, B., Li, S.C., Wang, J., Zhang, X.Q., Qi, S.H., 2009. Wenchuan Ms8.0 earthquake: preliminary study of the S-wave velocity structure of the crust and upper mantle. *Chinese Journal of Geophysics (in Chinese)* 52 (2), 309–319. http://www.geophy.cn/article/id/cjg_912.
- Liu, Q.Y., Van Der Hilst, R.D., Li, Y., Yao, H.J., Chen, J.H., Guo, B., Qi, S.H., Wang, J., Huang, H., Li, S.C., 2014. Eastward expansion of the Tibetan Plateau by crustal flow and strain partitioning across faults. *Nat. Geosci.* 7 (5), 361–365. <https://doi.org/10.1038/ngeo2130>.
- Liu, Y., Holt, W.E., 2015. Wave gradiometry and its link with Helmholtz equation solutions applied to USArray in the eastern U.S. *Journal of Geophysical Research: Solid Earth* 120 (8), 5717–5746. <https://doi.org/10.1002/2015JB011982>.
- Liu, Y., Li, L., van Wijk, J., Li, A., Fu, Y.V., 2021a. Surface-wave tomography of the Emeishan large igneous province (China): Magma storage system, hidden hotspot track, and its impact on the Capitanian mass extinction. *Geology* 49 (9), 1032–1037. <https://doi.org/10.1130/G49055.1>.
- Liu, Z., Tian, X., Liang, X., Liang, C., Li, X., 2021b. Magmatic Underplating Thickening of the Crust of the Southern Tibetan Plateau Inferred from Receiver Function Analysis. *Geophys. Res. Lett.* 48 (17) <https://doi.org/10.1029/2021GL093754>.
- Liu, Z.Q., Liang, C., Hua, Q., Li, Y., Yang, Y., He, F., Fang, L., 2018. The Seismic potential in the Seismic Gap between the Wenchuan and Lushan Earthquakes Revealed by the Joint Inversion of Receiver Functions and Ambient Noise Data. *Tectonics* 37 (11), 4226–4238. <https://doi.org/10.1029/2018TC005151>.
- Long, F., Zhang, Z., Qi, Y., Liang, M., Ruan, X., Wu, W., Jiang, G., Zhou, L., 2020. Three dimensional velocity structure and accurate earthquake location in Changning-Gongxian area of southeast Sichuan. *Earth and Planetary Physics* 4 (2), 1–15. <https://doi.org/10.26464/eppl2020022>.
- Maeda, T., Nishida, K., Takagi, R., Obara, K., 2016. Reconstruction of a 2D seismic wavefield by seismic gradiometry. *Progress in Earth and Planetary Science* 3 (1). <https://doi.org/10.1186/s40645-016-0107-4>.
- Marone, F., Romanowicz, B., 2007. The depth distribution of azimuthal anisotropy in the continental upper mantle. *Nature* 447 (7141), 198–201. <https://doi.org/10.1038/nature05742>.
- Molnar, P., Tapponnier, P., 1975. Cenozoic tectonics of Asia: Effects of a continental collision. In: *Science* (Vol. 189, issue 4201, pp. 419–426). <https://doi.org/10.1126/science.189.4201.419>.
- Ni, J.F., Guzman-Speziale, M., Bevis, M., Holt, W.E., Wallace, T.C., Seager, W.R., 1989. Accretionary tectonics of Burma and the three-dimensional geometry of the Burma subduction zone. *Geology* 17 (1), 68–71. [https://doi.org/10.1130/0091-7613\(1989\)017%3C0068:ATOBAT%3E2.3.CO;2](https://doi.org/10.1130/0091-7613(1989)017%3C0068:ATOBAT%3E2.3.CO;2).
- Porter, R., Liu, Y., Holt, W.E., 2016. Lithospheric records of orogeny within the continental U.S. *Geophys. Res. Lett.* 43 (1), 144–153. <https://doi.org/10.1002/2015GL066950>.
- Robert, A., Pubellier, M., de Sigoye, J., Vergne, J., Lahfid, A., Cattin, R., Findling, N., Zhu, J., 2010. Structural and thermal characters of the Longmen Shan (Sichuan, China). *Tectonophysics* 491, 165–173. <https://doi.org/10.1016/j.tecto.2010.03.018>.
- Rowley, D.B., 1996. Rowley Age of initiation of collision between India and Asia. *Earth Planet. Sci. Lett.* 145 (96), 1–13. [https://doi.org/10.1016/S0012-821X\(96\)00201-4](https://doi.org/10.1016/S0012-821X(96)00201-4).
- Royden, L.H., Burchfiel, B.C., King, R.W., Wang, E., Chen, Z., Shen, F., Liu, Y., 1997. Surface deformation and lower crustal flow in eastern Tibet. *Science* 276 (5313), 788–790. <https://doi.org/10.1126/SCIENCE.276.5313.788>.
- Ruan, A., Wang, C., 2002. The upper mantle anisotropy in Yunnan area, China. *Acta Seismologica Sinica* 24 (3), 266–267. <https://link.springer.com/article/10.1007/s11589-002-0060-8>.
- Searle, M.P., Coward, M.P., Cooper, D.J.W., Rex, A.J., Rex, D., Jan, M.Q., Umak J., O. K., 1987. The closing of Tethys and the tectonics of the Himalaya. *Geol. Soc. Am. Bull.* 98 (6), 678–701. <http://pubs.geoscienceworld.org/gsa/gsabulletin/article-pdf/9/8/678/3434697/10016-7606-98-6-678.pdf>.
- Shapiro, N.M., Campillo, M., 2004. Emergence of broadband Rayleigh waves from correlations of the ambient seismic noise. *Geophys. Res. Lett.* 31 (7), 8–11. <https://doi.org/10.1029/2004GL019491>.
- Shi, L., Lou, H., Wang, Q., Lu, H., Xu, W., 2015. Gravity field characteristics and crust density structure in the Panxi region, China. *Chin. J. Geophys. (in Chinese)* 58 (7), 2402–2412. <https://doi.org/10.6038/cjg20150717>.
- Silver, P.G., Chan, W.W., 1991. Shear wave splitting and subcontinental mantle deformation. *J. Geophys. Res.* 96 (B10) <https://doi.org/10.1029/91JB00899>.
- Smith, M.L., Dahlen, F.A., 1975. The Azimuthal Dependence of Love and Rayleigh Wave Propagation in a slightly Anisotropic Medium. *J. Geophys. Res.* 80 (14), 1923. <https://doi.org/10.1029/jb080i014p01923>.
- Sol, S., Meltzer, A., Bürgmann, R., van der Hilst, R.D., King, R., Chen, Z., Koons, P.O., Lev, E., Liu, Y.P., Zeitler, P.K., Zhang, X., Zhang, J., Zurek, B., 2007. Geodynamics of the southern Tibetan Plateau from seismic anisotropy and geodesy. *Geology* 35 (6), 563–566. <https://doi.org/10.1130/G23408A.1>.
- Sollberger, D., Schmelzbach, C., Robertsson, J.O.A., Greenhalgh, S.A., Nakamura, Y., Khan, A., 2016. The shallow elastic structure of the lunar crust: New insights from seismic wavefield gradient analysis. *Geophys. Res. Lett.* 43 <https://doi.org/10.1002/2016GL070883>.
- Tanimoto, T., Rivera, L., 2008. The ZH ratio method for long-period seismic data: Sensitivity kernels and observational techniques. *Geophys. J. Int.* 172 (1), 187–198. <https://doi.org/10.1111/j.1365-246X.2007.03609.x>.
- Tapponnier, P., Molnar, P., 1977. Active faulting and tectonics in China. *J. Geophys. Res.* 82 (20), 2905–2930. <https://doi.org/10.1029/jb082i020p02905>.
- Tapponnier, P., Peltzer, G., Le Dain, A.Y., Armijo, R., Cobbold, P., 1982. Propagating extrusion tectonics in Asia: new insights from simple experiments with plasticine. *Geology* 10 (12), 611–616. [https://doi.org/10.1130/0091-7613\(1982\)10<611:PETIAN>2.0.CO;2](https://doi.org/10.1130/0091-7613(1982)10<611:PETIAN>2.0.CO;2).
- Tapponnier, P., Zhiqin, X., Roger, F., Meyer, B., Arnaud, N., Wittlinger, G., Jingsui, Y., 2001. Oblique stepwise rise and growth of the Tibet plateau. In: *Science* (Vol. 294, issue 5547, pp. 1671–1677). <https://doi.org/10.1126/science.105978>.
- Wang, C.Y., Flesch, L.M., Silver, P.G., Chang, L.J., Chan, W.W., 2008. Evidence for mechanically coupled lithosphere in Central Asia and resulting implications. *Geology* 36 (5), 363–366. <https://doi.org/10.1130/G24450A.1>.
- Wang, H.F., Wu, J., Zhou, S., Feng, T., 2020. Rayleigh wave azimuthal anisotropy in western Sichuan region. *Acta Seismol. Sin.* 42 (3), 293–305. <https://doi.org/10.11939/jass.20190103>.
- Wang, L.Q., Pan, G.T., Ding, J., Yao, D.S., 2013b. Geological Map of Tibetan Plateau and its Surrounding Area at 1/1,500,000: Beijing. Geol. Publ. House.
- Wang, N., Montagner, J.P., Fichtner, A., Capdeville, Y., 2013a. Intrinsic versus extrinsic seismic anisotropy: the radial anisotropy in reference Earth models. *Geophys. Res. Lett.* 40 (16), 4284–4288. <https://doi.org/10.1002/grl.50873>.
- Wang, W., Wu, J., Hammond, J.O.S., 2021. Mantle Dynamics beneath the Sichuan Basin and Eastern Tibet from Teleseismic Tomography. *Tectonics* 40 (2), 1–16. <https://doi.org/10.1029/2020TC006319>.
- Wang, Z., Su, J., Liu, C., Cai, X., 2015. New insights into the generation of the 2013 Lushan Earthquake (Ms 7.0), China. *Journal of Geophysical Research: Solid Earth* 120 (5), 3507–3526. <https://doi.org/10.1002/2014JB011692>.
- Xia, Z.S., 1982. Continental Mesozoic Stratigraphy and Paleontology in Sichuan Basin of China. Geologic Publishing House, Beijing, pp. 1–734.
- Xu, B., 1997. The tectonic reversion in the early Yanshanian stage and forming of embryonic form of Weiyuan anticline in Weiyuan area, Sichuan. *J. Mineral Petrol* 17 (2), 44–48. <https://doi.org/10.19719/j.cnki.1001-6872.1997.03.009>.
- Xu, Q., Ding, L., Zhang, L., Cai, F., Lai, Q., Yang, D., Liu-Zeng, J., 2013. Paleogene high elevations in the Qiangtang Terrane, central Tibetan Plateau. *Earth Planet. Sci. Lett.* 362, 31–42. <https://doi.org/10.1016/j.epsl.2012.11.058>.
- Xu, T., Zhang, Z., Liu, B., Chen, Y., Zhang, M., Tian, X., Xu, Y., Teng, J., 2015. Crustal velocity structure in the Emeishan large igneous province and evidence of the

- Permian mantle plume activity. *Sci. Sin. Terra* 45 (5), 561–576. <https://doi.org/10.1360/zd-2015-45-5-561>.
- Xu, X., Wen, X., Zheng, R., Ma, W., Song, F., Yu, G., 2003. Pattern of latest tectonic motion and its dynamics for active blocks in Sichuan-Yunnan region, China. *Sci. China Ser. D Earth Sci.* 46 (SUPP), 210–226. <https://doi.org/10.1360/03yd9020>.
- Yang, Y.H., Liang, C., Li, Z., Su, J., Zhou, L., He, F., 2017. Stress distribution near the Seismic Gap between Wenchuan and Lushan Earthquakes. *Pure Appl. Geophys.* 174 (6), 2257–2267. <https://doi.org/10.1007/s00024-016-1360-6>.
- Yang, Y.H., Liang, C., Fang, L., Su, J., Hua, Q., 2018. A Comprehensive Analysis on the stress Field and Seismic Anisotropy in Eastern Tibet. *Tectonics* 37 (6), 1648–1657. <https://doi.org/10.1029/2018TC005011>.
- Yang, Y.H., Zhang, X., Dong, Y., Sun, S., Hua, Q., Liang, C., 2022. Crustal Deformation patterns in the Tibetan Plateau and its Adjacent Regions as Revealed by Receiver Functions. *Bulletin of the Seismological Society of America*, Xx 1–18. <https://doi.org/10.1785/0120210228>.
- Yang, Y.J., Forsyth, D.W., 2006. Regional tomographic inversion of the amplitude and phase of Rayleigh waves with 2-D sensitivity kernels. *Geophys. J. Int.* 166 (3), 1148–1160. <https://doi.org/10.1111/j.1365-246x.2006.02972.x>.
- Yang, Y.J., Shen, W., Ritzwoller, M.H., 2011. Surface wave tomography on a large-scale seismic array combining ambient noise and teleseismic earthquake data. *Earthquake Science* 2011 24:1 24 (1), 55–64. <https://doi.org/10.1007/S11589-011-0769-3>.
- Yao, H., van der Hilst, R.D., de Hoop, M.V., 2006. Surface-wave array tomography in SE Tibet from ambient seismic noise and two-station analysis - I. Phase velocity maps. *Geophysical Journal International* 166 (2), 732–744. <https://doi.org/10.1111/j.1365-246x.2006.03028.x>.
- Yao, H., Van Der Hilst, R.D., Montagner, J.P., 2010. Heterogeneity and anisotropy of the lithosphere of SE Tibet from surface wave array tomography. *Journal of Geophysical Research: Solid Earth* 115 (12), 1–24. <https://doi.org/10.1029/2009JB007142>.
- Yin, A., 2010. A special issue on the great 12 May 2008 Wenchuan earthquake (Mw7.9): Observations and unanswered questions. *Tectonophysics* 491, 1–9. <https://doi.org/10.1016/j.tecto.2010.05.019>.
- Yin, A., Harrison, T.M., 2000. Geologic evolution of the Himalayan-Tibetan Orogen. *Annual Reviews of Earth and Planetary Sciences* 28, 211–280. <https://doi.org/10.1146/annurev.earth.28.1.211>.
- Yuan, H., Romanowicz, B., 2010. Lithospheric layering in the north American craton. *Nature* 466 (7310), 1063–1068. <https://doi.org/10.1038/nature09332>.
- Yuan, H., Romanowicz, B., Fischer, K.M., Abt, D., 2011. 3-D shear wave radially and azimuthally anisotropic velocity model of the north American upper mantle. *Geophys. J. Int.* 184 (3), 1237–1260. <https://doi.org/10.1111/j.1365-246X.2010.04901.x>.
- Zhang, P., 2008. The current tectonic deformation, strain distribution and deep dynamic process in the Western Sichuan-Tibet Plateau (in Chinese). *Science China Earth Sciences* 38 (9), 1041–1056. <https://doi.org/10.1360/zd2008-38-9-1041>.
- Zhang, P.Z., Deng, Q.D., Zhang, Z.Q., Li, H.B., 2013. The current tectonic deformation, strain distribution and deep dynamic process in the Western Sichuan-Tibet Plateau (in Chinese). *Science China Earth Sciences* 43 (10), 1607–1620. <https://doi.org/10.1360/zd-2013-43-10-1607>.
- Zhang, R., 2018. Petrogenesis of the Genozoic Alkaline Potassic-Ultrapotassic Volcanic Rocks from Qiangtang, Northern Tibet (in Chinese). Doctor Dissertation. Jilin University, Jilin.
- Zhang, Z., Yao, H., Yang, Y., 2020. Shear wave velocity structure of the crust and upper mantle in Southeastern Tibet and its geodynamic implications. *Science. Science China Press* 50 (9), 1242–1258. <https://doi.org/10.1360/sste-2020-0016>.
- Zhang, Z., Yao, H., Wang, W., Liu, C., 2021. 3-D crustal azimuthal anisotropy reveals multi-stage deformation processes of the Sichuan Basin and its adjacent area, SW China. *Journal of Geophysical Research: Solid Earth* 1–17. <https://doi.org/10.1029/2021jb023289>.
- Zhao, B., Huang, Y., Zhang, C., Wang, W., Tan, K., Du, R., 2015. Crustal deformation on the Chinese mainland during 1998–2014 based on GPS data. *Geodesy and Geodynamics* 6 (1), 7–15. <https://doi.org/10.1016/j.geog.2014.12.006>.
- Zhao, L., Zheng, T., Chen, L., Tang, Q., 2007. Shear wave splitting in eastern and Central China: Implications for upper mantle deformation beneath continental margin. *Phys. Earth Planet. Inter.* 162 (1–2), 73–84. <https://doi.org/10.1016/j.pepi.2007.03.004>.
- Zhao, L., Zheng, T., Lu, G., 2013. Distinct upper mantle deformation of cratons in response to subduction: Constraints from SKS wave splitting measurements in eastern China. *Gondwana Res.* 23 (1), 39–53. <https://doi.org/10.1016/j.gr.2012.04.007>.
- Zheng, T., Ding, Z., Ning, J., Chang, L., Wang, X., Kong, F., Liu, K.H., Gao, S.S., 2018. Crustal Azimuthal Anisotropy beneath the Southeastern Tibetan Plateau and its Geodynamic Implications. *Journal of Geophysical Research: Solid Earth* 123 (11), 9733–9749. <https://doi.org/10.1029/2018JB015995>.
- Zhou, L., Liang, C., Yang, Y., 2017. Application of three-component seismic-wave gradiometry for the Central and Eastern United States. *Chin. J. Geophys.* <https://doi.org/10.6038/cjg20170907>.
- Zhu, L., Kanamori, H., 2000. Moho depth variation in southern California from teleseismic receiver functions. In *Journal of Geophysical Research: Solid. Earth* 105 (B2), 2969–2980. <https://doi.org/10.1029/1999jb900322>.